



CO oxidation and NO reduction by CO over Sn⁴⁺ doped CeO₂ catalysts: Determination of active sites as well as commonness and differences

Changshun Deng ^{a,*}, Xiaofeng Qian ^a, Minping Lu ^b, Qing Liu ^a, Taotao Zhao ^a, Jie Yang ^a, Teng Chen ^{a,c,**}, Lin Dong ^{a,d,e,**}

^a Key Lab of Mesoscopic Chemistry, School of Chemistry and Chemical Engineering, Nanjing University, Nanjing 210023, China

^b Guangxi Zhuang Autonomous Region Institute of Metrology & Test, Nanning 530200, China

^c Department of Aviation Oil and Material, Air Force Logistics Academy, Xuzhou 221000, China

^d State Key Laboratory of Pollution Control and Resource Reuse, School of the Environment, Nanjing University, Nanjing 210023, China

^e Jiangsu Key Laboratory of Vehicle Emissions Control, Center of Modern Analysis, Nanjing University, Nanjing 210023, China



ARTICLE INFO

Keywords:

Sn⁴⁺ doped CeO₂
CO oxidation
NO + CO reaction
Formation energy of oxygen vacancy
Reaction mechanism

ABSTRACT

Sn doping sites in CeO₂ can greatly affect its electronic structures. However, the identification of adsorption/active sites, their effects on CO oxidation and NO reduction by CO, and the commonness and differences between the two reactions have never been addressed. Herein, Sn⁴⁺ is selectively doped into nano-rod and nano-cubic CeO₂ by hydrothermal methods. It is found that the Ce₁₀Sn₁O₉ catalysts exhibit greatly promotional effects on both the two reactions, which benefits from the formation of more oxygen vacancies (OVs), stronger redox ability that can enhance the mobility of lattice oxygen, lower formation energies of OVs, and weaker alkalinity that can increase the desorption of product CO₂. Experiments and DFT calculations show that they share the same adsorption/active site, i.e., Sn²⁺-O_v-Ce³⁺, in the two reactions. Meanwhile, the CO oxidation half-reaction has obvious dependence on the active [O] species derived from the dissociation of NO species during NO reduction by CO.

1. Introduction

Increasingly serious air pollution and global warming are threatening human health and the global environment, and building a low-carbon society has become a worldwide topic [1]. Among various emitted toxic pollutants, the emission of nitrogen oxides (NO_x), mainly emitted by mobile resources and stationary resources, is one of the main causes of air pollution [2]. Therefore, the emission regulations of NO_x are becoming more and more strict and the removal technologies of this pollutant is widely concerned around the world [3]. Among many methods of eliminating NO_x, selective catalytic reduction (SCR) is one of the most effective technologies to remove NO_x using CO, hydrocarbons (C_xH_y), or NH₃ as reducing agents [4]. Although platinum group metal catalysts, such as Ir, Rh, Pd, and Pt, display superior pollutant removal efficiency, scarcity and high prices limit their practical applications [5]. Thus, it is very necessary to develop noble metals-free catalysts for the elimination of NO_x in both scientific researches and industrial applications [6].

Ceria, an important rare earth material, widely applied in the fields of energy, environment, and catalysis due to superexcellent oxygen storage capability (OSC) and promising redox properties [7–9]. Pure ceria, however, has poor thermal stability as well as impressionable sintering at high temperature which leads to its deactivation [1,8,10]. Another disadvantage is that ceria has poor low-temperature activity in many reactions including CO oxidation and NO reduction by CO (NO + CO reaction) [4,11]. It is generally accepted that the doping of foreign metal cations into the unit cell of ceria can significantly increase the catalytic performance due to the enhanced redox behavior and oxygen vacancies (OVs) [12]. In addition, the thermal stability of ceria-based materials is often much better than that of pure ceria [13].

In recent decades, to further guide the design of more useful catalyst for CO oxidation and NO + CO reaction, numerous contributions have been made to elucidate the active sites and unlock the corresponding reaction mechanism [1–4,8,14–16]. For example, Dong et al. concluded that in the intergrowth process of CuO and CeO₂, the strong interaction between them induced an imperfect [Cu_{1-x}²⁺Cu_x⁺][O_{1-x/2}□_{x/2}] structure

* Corresponding author.

** Corresponding authors at: Key Lab of Mesoscopic Chemistry, School of Chemistry and Chemical Engineering, Nanjing University, Nanjing 210023, China.

E-mail addresses: dengcs@nju.edu.cn (C. Deng), chentyp@yeah.net (T. Chen), donglin@nju.edu.cn (L. Dong).

which greatly increased the catalytic performances in CO oxidation and NO + CO reaction [14]. Li et al. found that macroporous CeO₂-ZrO₂ oxides exhibited much better catalytic activity than that of macroporous CeO₂ for CO oxidation, because the former generated more OVs [15]. Similar results reported by Liu et al. had also been found that the doping of Fe₂O₃ into CeO₂ efficiently tuned the Ce⁴⁺/Ce³⁺ redox couple and increased the concentration of OVs for NO + CO reaction [16]. Other ceria-based materials with various dopants, such as CeO₂-Al₂O₃ [17], CeO₂-Co₃O₄ [18], CeO₂-TiO₂ [19], CeO₂-CrO_x [4], and CeO₂-SnO₂ [20] have also been reported highly active in many reactions. Among the foreign components, SnO₂, a highly concerned semiconductor gas sensor material and heterogeneous catalyst, possesses abundant intrinsic defects and can produce OVs due to the easy reversibility between Sn⁴⁺ and Sn²⁺ at a relatively low temperature [21,22]. Both Dong and Bin et al. found that the doping of SnO₂ into CeO₂ increased the thermal stability of the catalysts and the active sites were closely related to the synergistic interaction of Sn²⁺ + 2Ce⁴⁺ ↔ Sn⁴⁺ + 2Ce³⁺ for NO + CO reaction [20,23]. Similarly, the introduction of SnO₂ into the CeO₂-TiO₂ composites increased the amount of chemisorbed oxygen, reported by Li et al., displaying marvelous resistance to the poisoning of H₂O and SO₂ for NO reduction by NH₃ [24].

Based on the above studies, however, there are still some research limitations and problems to be solved. Firstly, in previous works, the doping proportion of foreign components in ceria is often not low, which may result in the loss of some original main structure in ceria, thus increasing the complexity of theoretical modeling calculation and difficulty in determining active sites. Secondly, most of the studies focus on the doping of ceria nanoparticles, while the researches on the doping of ceria nanorods and nanocubes are less without changing the morphologies. After all, the catalytic performances of ceria nanorods and nanocubes are better than that of ceria nanoparticles in both CO oxidation and NO + CO reaction. Thirdly, the doping of multivalent metals will easily promote the electron transfer of ceria due to the volatility of valence state, thus increasing the catalytic performance. However, the identification of active sites and the revelation of reaction mechanism are still relatively lacking in the above reactions. In addition, NO + CO reaction involves two half-reactions: CO oxidation and NO reduction. For CO oxidation, adsorbed CO on metal cation active sites is oxidized by active oxygen species formed by OVs [20]; for NO reduction, the dissociation of NO is the key step and it is generally believed that the N-O bond can be activated by OVs to promote the dissociation of NO species [1,4,23]. Moreover, it should be emphasized that the CO oxidation half-reaction exhibits high dependence on the active oxygen species derived from the dissociation of NO species during NO + CO reaction [25]. Connected and inspired by these mechanisms, it is highly probable that CO oxidation and NO + CO reaction share the same active sites. Therefore, the two reactions are closely related in the reaction process, although they are two different reactions. Studying the above two reactions together is helpful to further understand and determine the active sites, which is very important for the guidance and design of efficient and well-defined heterogeneous catalysts. In addition, to the best of our knowledge, the synthesis of CeO₂-SnO₂ composite oxides with different morphologies in doping effect and understanding of mechanism on CO oxidation and NO + CO reaction were scarcely reported.

Herein, new CeO₂-SnO₂ catalysts with the morphologies of nanorod and nanocube were synthesized and the doped catalysts exhibited excellent catalytic performances in CO oxidation and NO + CO reaction compared to pure CeO₂ catalysts. Based on the commonness and differences of the catalytic performances of the above catalysts in CO oxidation and NO + CO reaction, four aspects of in-depth investigations were carried out to reveal these reasons: (1) effect of catalyst structure modification on catalytic performances and reaction kinetics; (2) effect of Sn⁴⁺ doping on the structure evolution of CeO₂ (nanorod and nanocube); (3) identification of adsorption/active sites and determination of local coordination environment, and (4) revelation of reaction

mechanisms as well as their similarities and differences. The objective of this work is to provide an uncomplicated strategy for the design and synthesis of noble metals-free catalysts in vehicle emission control, and take an understanding of CO oxidation and NO + CO reaction on Sn⁴⁺ doped ceria-based catalysts a step forward.

2. Materials and methods

2.1. Catalyst preparation

CeO₂-SnO₂ composite oxides (the molar ratio of Ce/Sn is 10: 1) with different morphologies were synthesized by a hydrothermal method [26]. Typically, 5 mmol of Ce(NO₃)₃·6H₂O and 0.5 mmol of SnCl₄·5H₂O were dissolved in 20 mL of distilled water, which was labeled as A; 0.48 mol of NaOH was dissolved in 40 mL of distilled water, which was labeled as B. Then, A was added into B drop by drop with vigorous stirring. After stirring for 1 h, the mixture was transferred into a Teflon autoclave (100 mL) and kept for 24 h at appropriate temperatures (100 °C for nanorods and 180 °C for nanocubes). Then, the mixture was centrifugated and washed with deionized water and absolute alcohol for 3 times, respectively, and the precipitate was dried at 80 °C for about 12 h and then calcined at 400 °C for 4 h in air with a heating rate of 2 °C·min⁻¹. Pure CeO₂ with different morphologies were synthesized with similar method. The prepared nanorods of CeO₂ and CeO₂-SnO₂ were denoted as CeO₂-r and Ce₁₀Sn₁O_x-r; the prepared nanocubes of CeO₂ and CeO₂-SnO₂ were denoted as CeO₂-c and Ce₁₀Sn₁O_x-c, respectively.

2.2. Catalyst characterization

Thermogravimetric analysis and derivative thermogravimetry (TG-DTA) measurements were carried out on a STA 449 C apparatus in air from ambient temperature to 800 °C with a heating rate of 10 °C·min⁻¹. X-ray diffraction (XRD) patterns were performed on an X'pert PAN analytical diffractometer with the Cu K α (40 kV and 40 mA) radiation. The textural characteristics of these catalysts were tested at -196 °C using a Micrometrics TriStar II 3020 analyzer. Raman patterns were performed on a Renishaw Invia spectrometer equipped with a laser radiating at 532 nm. The UV/Vis diffuse reflectance spectroscopy (DRS) spectra were obtained on a TU-1901 spectrophotometer (Shimadzu) in the wavelength range of 200–800 nm, BaSO₄ was used as the reference material. Transmission electron microscopy (TEM) and high resolution transmission electron microscopy (HRTEM) images were measured on a JEOL JEM-2100 system (200 kV).

Both hydrogen temperature-programmed reduction (H₂-TPR) and carbon dioxide temperature-programmed desorption (CO₂-TPD) results were tested on a Tianjin XQ TPS080 chemisorption instrument. For H₂-TPR, the sample was first pretreated in the flowing of helium at 300 °C for 1 h, then TPR signal was recorded from 30 to 550 °C in 5 vol% H₂/N₂, the heating rate was set as 10 °C·min⁻¹. For CO₂-TPD, the sample was first pretreated in the flowing of helium at 300 °C for 1 h, then it was cooled to room temperature in helium. After that, it was contacted with CO₂ at room temperature for 0.5 h and then was purged by helium to remove residual CO₂. Then TPD signal was recorded from 30 to 800 °C in helium, the heating rate was set as 10 °C·min⁻¹. Electron paramagnetic resonance (EPR) spectra were tested on a Bruker EMX system at 20 K. Inductively coupled plasma-atomic emission spectrometry (ICP-AES) measurements were conducted on an instrument of Optima 5300 DV (PerkinElmer) equipped with a radiofrequency power of 1300 W. X-ray photoelectron spectroscopy (XPS) spectra were measured on a PHI 5000 VersaProbe equipped with an Al K α excitation source.

In situ DRIFTS spectra were performed on a Nicolet iS50 DRIFTS spectrometer. Firstly, the catalyst was added into the quartz IR cell and pretreated for 1 h at 400 °C in nitrogen and then cooled to room temperature. Secondly, the spectra were gathered at multiple set temperatures as background. Thirdly, the catalyst was exposed to controlled

stream of 10 vol% CO/Ar, 10 vol% CO/Ar and 20 vol% O₂/Ar, 5 vol% NO/Ar, and 10 vol% CO/Ar and 5 vol% NO/Ar with a rate of 10 mL·min⁻¹ for 0.5 h, respectively. Finally, the IR spectra were collected in different atmospheres, from room temperature to 400 °C with an interval of 25 °C.

2.3. Catalytic tests

A continuous flow fixed-bed micro-reactor equipped with a quartz tube reactor with an internal diameter of 4 mm was used for the performance evaluation of the two catalytic reactions. For CO oxidation, the reactants were comprised of 2 vol% CO, 5 vol% O₂, and 93 vol% Ar; for NO + CO reaction, the reactants consisted of 5 vol% NO, 10 vol% CO, and 85 vol% Ar. Additionally, 5 vol% water will be added into the reaction system when necessary. In the two catalytic reactions, both the amount of catalyst added was 50 mg and the weight hourly space velocity (WHSV) was 24,000 mL·g⁻¹·h⁻¹. Both the outlet gas compositions in the two catalytic reactions were detected by online GC-9860 gas chromatograph equipped with two thermal conductivity detectors (Paropak Q and 5 A molecular sieves columns). Paropak Q column was used to separate CO₂ and N₂O; 5 A molecular sieves column was used to separate N₂, NO, and CO.

In addition, the CO conversion in CO oxidation and NO + CO reaction as well as NO conversion, N₂ selectivity, and N₂ yield in NO + CO reaction were calculated according to the following formulas, respectively:

$$X_{CO} = \frac{CO_{in} - CO_{out}}{CO_{in}} \times 100\%$$

$$X_{NO} = \frac{NO_{in} - NO_{out}}{NO_{in}} \times 100\%$$

$$S_{N_2} = \frac{2N_2}{NO_{in} - NO_{out}} \times 100\%$$

$$Y_{N_2} = X_{NO} \times S_{N_2}$$

where CO_{in} (or NO_{in}) and CO_{out} (or NO_{out}) represent the molar fraction of CO (or NO) at the inlet and outlet, respectively.

2.4. Computational methods

In this work, all the calculated results were attained through the first-principle method with the Cambridge serial total energy package (CASTEP) module in Materials Studio [27]. The calculations are performed using the density functional theory (DFT) with the Perdew-Burke-Ernzerhof (PBE) functional based on generalized gradient approximation (GGA). The cutoff energy of atomic wave functions was set as 630 eV. The k point was set as 1 × 1 × 1. The atom positions were relaxed using the Broyden-Fletcher-Goldfarb-Shanno (BFGS) method [28]. All structures were fully relaxed without any symmetry constraint. The structural optimization parameters were as follows: Energy, Max. force, and Max. displacement were set as 1.0e⁻⁵ eV/Å, 0.03 Ha/Å, and 0.001 Å, respectively.

CeO₂ is a cubic crystal, the space group is Fm-3 m (225), the lattice parameter of the crystal is a = b = c = 5.411 Å, and the crystal contains four Ce atoms and eight O atoms. When constructing a CeO₂ surface model, the most stable crystal plane ({1 1 1} plane) of CeO₂ was used for modeling. A 5-layer structure was selected and the surface model was supercellular treated (2 × 2) with the addition of a 15 Å vacuum layer. The position of the atoms was not fixed and sufficient relaxation was carried out on the atoms to achieve a stable state of the crystal during the calculation process.

3. Results and discussion

3.1. Catalytic performances of CeO₂–SnO₂ catalysts

The catalytic performances of CO oxidation over the CeO₂–SnO₂ catalysts were firstly conducted and shown in Fig. 1a-c and Fig. S1. It is obvious that the catalytic performance of CeO₂-r (rods, T₅₀ = 268 °C, T₅₀ refers to the temperature when the conversion of CO oxidation reaches 50%) is much better than that of CeO₂-c (cubes, T₅₀ = 360 °C), in agreement with previous work [29]. Excitingly, both the great leaps in catalytic performance can be observed on Ce₁₀Sn₁O_x-r (T₅₀ = 218 °C) and Ce₁₀Sn₁O_x-c (T₅₀ = 278 °C) when a little SnO₂ is added into CeO₂, compared to CeO₂-r and CeO₂-c, in which Ce₁₀Sn₁O_x-r exhibits the best catalytic performance of CO oxidation (Fig. 1a). From the perspective of dynamics, the apparent activation energies (Fig. 1b) of CeO₂-r and Ce₁₀Sn₁O_x-r are ca. 51 and 55 kJ·mol⁻¹, respectively, which are much lower than those of CeO₂-c and Ce₁₀Sn₁O_x-c (ca. 94 and 91 kJ·mol⁻¹, respectively). Moreover, the CO oxidation reaction rates for Ce₁₀Sn₁O_x-r and other catalysts are 6.04 μmol_{CO}·g_{cat}⁻¹·s⁻¹ at 225 °C and lower than 1.45 μmol_{CO}·g_{cat}⁻¹·s⁻¹ at 225 or 275 °C, respectively (Fig. 1c); the value of Ce₁₀Sn₁O_x-r is 4–13 times higher than those of other catalysts. In addition, the stable long-term tests of Ce₁₀Sn₁O_x-r and Ce₁₀Sn₁O_x-c demonstrate the stable structure of them (Fig. S1). Moreover, the T₅₀, T₉₀, and relevant kinetic data have also been summarized and listed in Table S1.

Secondly, the CeO₂–SnO₂ catalysts were applied in NO + CO reaction, which was one of principal model reactions in the gasoline vehicle exhaust purification system [25,30], as shown in Fig. 1d-i and Figs. S2–4. It is very similar to the results in CO oxidation that the NO conversion of CeO₂-r (T₅₀ = 312 °C) is much better than that of CeO₂-c (T₅₀ = 405 °C) and the addition of a little SnO₂ into CeO₂ greatly increases the activity with a T₅₀ of 265 °C on Ce₁₀Sn₁O_x-r and a T₅₀ of 324 °C on Ce₁₀Sn₁O_x-c (Fig. 1d). Likewise, the Ce₁₀Sn₁O_x-r also exhibits the best CO conversion, N₂ selectivity, and N₂ yield, especially below 300 °C (Fig. 1e-g). Meanwhile, much lower concentrations of N₂O can be detected on all catalysts compared to the concentrations of CO and NO, and Ce₁₀Sn₁O_x-r shows the lowest concentration of N₂O in higher temperature areas (> 250 °C) (Fig. S2), demonstrating that the appropriate addition of SnO₂ into CeO₂-r greatly inhibits the generation of N₂O or promotes the dissociation/transformation of N₂O to N₂. Moreover, the apparent activation energies (Fig. 1 h) of CeO₂-r and Ce₁₀Sn₁O_x-r are ca. 19 and 25 kJ·mol⁻¹, respectively, which are much lower than those of CeO₂-c and Ce₁₀Sn₁O_x-c (ca. 62 and 38 kJ·mol⁻¹, respectively). The above results reflected in the NO reaction rates are that the reaction rate of Ce₁₀Sn₁O_x-r is 2–3 times higher than those of other catalysts at 225 °C. The T₅₀ and relevant kinetic data have been summarized and listed in Table S2. The stable long-term tests of Ce₁₀Sn₁O_x-r and Ce₁₀Sn₁O_x-c in the presence of 5 vol% water demonstrate that a new stable and water resistant structure is constructed by the addition of SnO₂ into CeO₂ (Fig. S3). In addition, the catalytic performances at higher WHSV imply that the reaction trends of these catalysts at higher and lower WHSV are very similar, but their reaction activities at high WHSV is slightly lower than that at low WHSV (Fig. S4). Meanwhile, Ce₁₀Sn₁O_x-r also shows the best catalytic performances in NO + CO reaction.

On the basis of the above results in CO oxidation and NO + CO reaction over the typical catalysts, it can be found that the change trends of the CO conversions in CO oxidation and NO conversions in NO + CO reaction between these catalysts are very similar, implying that the active sites on these catalysts may be closely related to each other in CO oxidation and NO + CO reaction. In especial, the Ce₁₀Sn₁O_x-r shows the best catalytic activities in both reactions. However, the catalytic results alone are far from providing a thorough and clear insight into the relationships between catalyst structure and performance. Therefore, the commonness and otherness of the active sites on the catalysts in CO oxidation and NO + CO reaction and the structural evolution from CeO₂

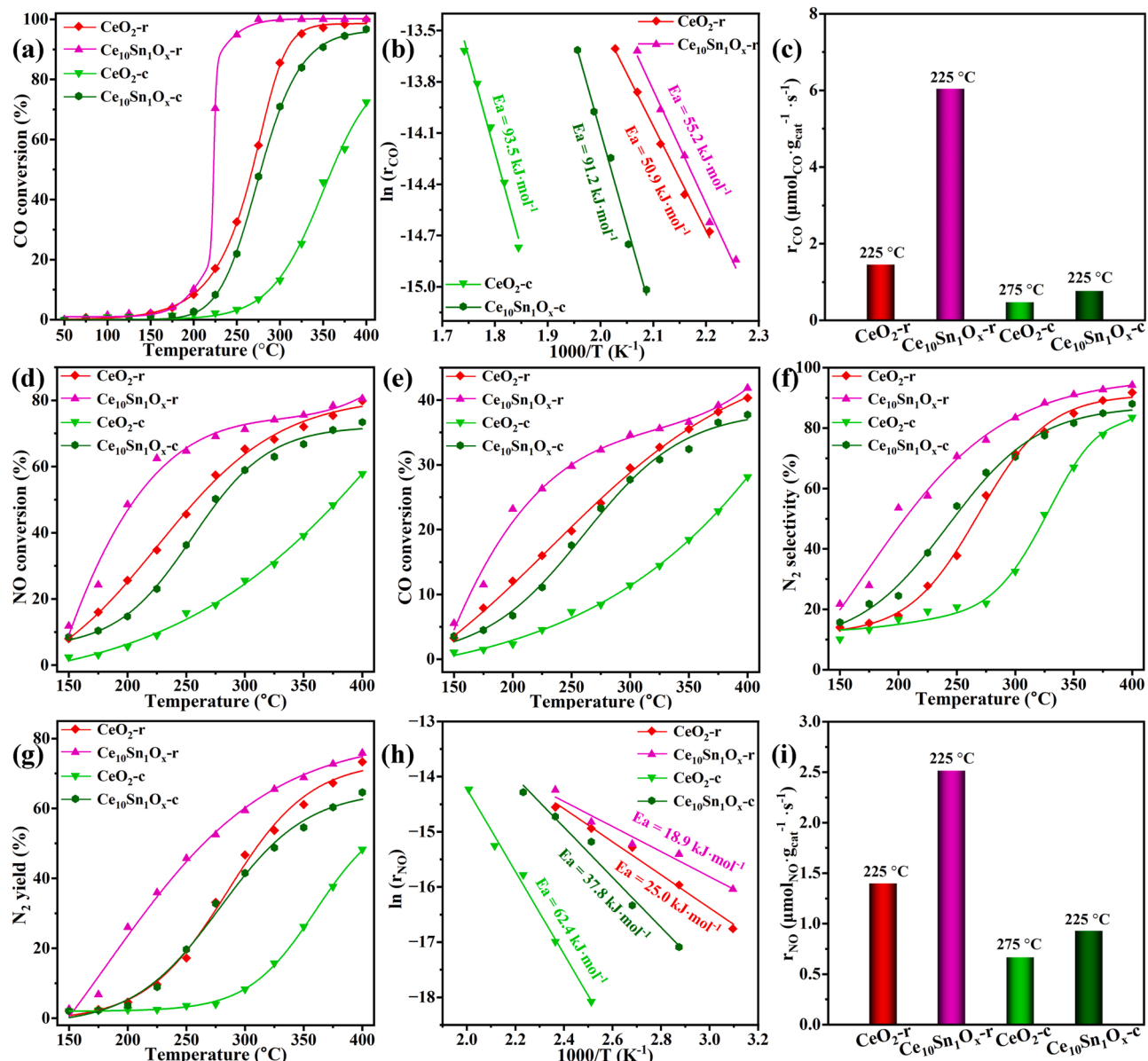


Fig. 1. (a-c) The catalytic performance, Arrhenius plots, and CO reaction rates for CO oxidation over typical catalysts, respectively (2 vol% CO, 5 vol% O₂, and 93 vol % Ar; cat. = 50 mg; WHSV = 24,000 mL·g⁻¹·h⁻¹). (d-i) The catalytic performances (NO and CO conversion, N₂ selectivity, and N₂ yield, respectively), Arrhenius plots, and NO reaction rates for NO + CO reaction over typical catalysts, respectively (5 vol% NO, 10 vol% CO, and 85 vol% Ar; cat. = 50 mg; WHSV = 24,000 mL·g⁻¹·h⁻¹).

to Ce₁₀Sn₁O_x will be detailedly investigated in the following sections.

3.2. Structural properties of CeO₂–SnO₂ catalysts

In the TG results (Fig. S5), there is almost no mass loss after 400 °C, indicating that the precursor salts of cerium and tin can be completely calcined into CeO₂–SnO₂ composite oxides in air at this temperature. The XRD patterns shown in Fig. 2a indicate that all catalysts only display a cubic fluorite-type structure of CeO₂ (PDF-ICDD 34–0394), and the characteristic peaks ascribed to SnO₂ are completely absent. It is very important that both the diffraction angles ascribed to Ce₁₀Sn₁O_x-r and Ce₁₀Sn₁O_x-c shift to a higher angle compared to CeO₂-r and CeO₂-c, indicating that Sn⁴⁺ has been well doped into the lattice of CeO₂, thus resulting in the shrinkage of unit cell [1,19,31]. Similarly, the results of crystallite sizes determined by XRD demonstrate that the crystallite sizes of Ce₁₀Sn₁O_x decrease compared to CeO₂ (Table S3). The N₂ sorption isotherms (Fig. 2b) reveal that all catalysts display the IV-type isotherms

with evident H3-type hysteresis loops [32–34], but the hysteresis loops of nanorod catalysts are much bigger than those of cube catalysts, suggesting the larger pore volumes in former (Table S3). Interestingly, the textural parameters (Fig. 2b and Table S3) of Ce₁₀Sn₁O_x-r and Ce₁₀Sn₁O_x-c are almost the same with those of CeO₂-r and CeO₂-c, respectively, demonstrating that the doping of SnO₂ into CeO₂ has an almost negligible effect on the main structure of CeO₂.

In Raman spectra (Fig. 2c), CeO₂-r and CeO₂-c exhibit a main band at ca. 464 and 463 cm⁻¹ (labeled as II), respectively, which is ascribed to the F_{2g} vibration model of the cubic fluorite-type lattice of CeO₂ [31,35]. However, the position of this band is shifted to ca. 462 and 465 in Ce₁₀Sn₁O_x-r and Ce₁₀Sn₁O_x-c, respectively, indicating that Sn⁴⁺ has been incorporated into the lattice of CeO₂ to form composite oxide, in agreement with XRD results [4]. This is because the lattice of CeO₂ is distorted by the incorporation of Sn⁴⁺, leading to an obvious effect on the polarizability of the symmetrical stretching mode of the [Ce–O₈] vibrational unit and thus causing the skewing of the band [36].

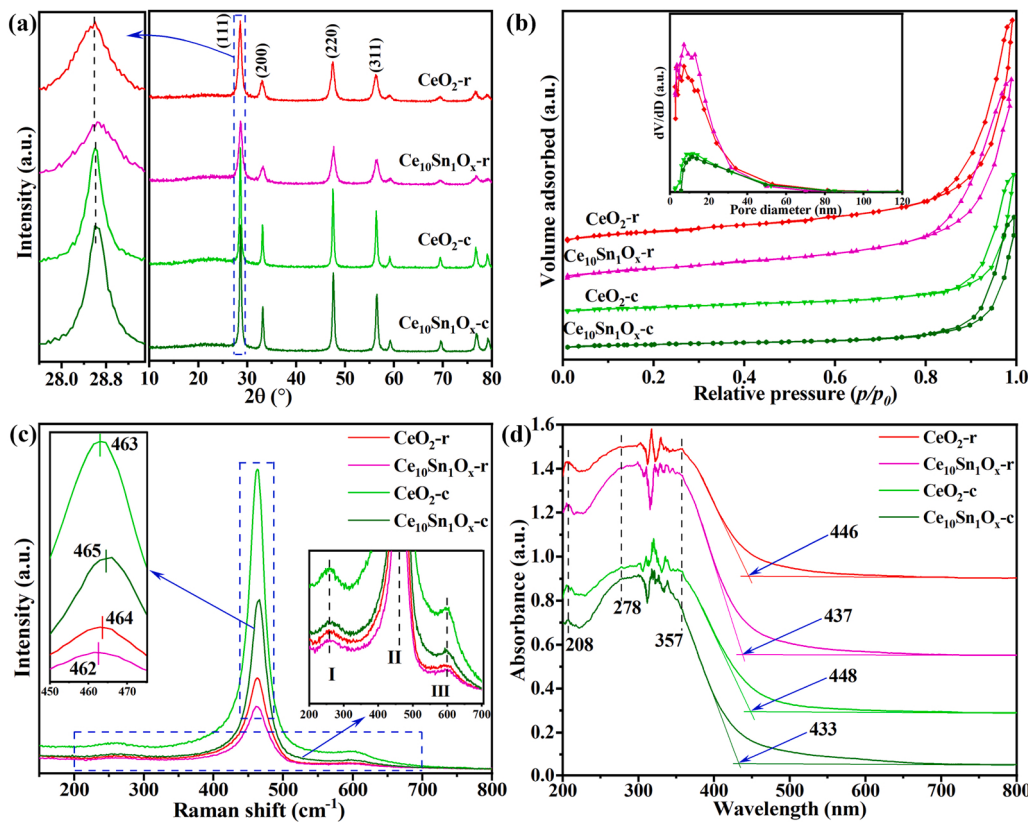


Fig. 2. The XRD patterns (a), N₂ sorption isotherms and BJH pore size distribution curves (inset) (b), Raman spectra (c), and UV-vis DRS spectra of typical catalysts.

Furthermore, the other two bands appeared at ca. 257 and 599 cm⁻¹ (labeled as I and III, respectively) are attributed to the substitution of oxygen atoms from their ideal fluorite lattice positions and nondegenerate LO mode of CeO₂ arising from relaxation of the symmetry rules, respectively [1,37]. Moreover, both the full-width at half maximum (FWHM) values of the F_{2g} bands in Ce₁₀Sn₁O_x-r and Ce₁₀Sn₁O_x-c are larger than those in CeO₂-r and CeO₂-c (Table S3), which may be related to the concentration of defects (such as OVs) and/or the crystallite size of these catalysts [4,38]. Besides, for Ce-based catalysts, the relative concentration of OVs can be expressed by the area ratio of (A_I + A_{III})/A_{II} [31,39], and the values shown in Table S3 imply that the incorporation of Sn⁴⁺ into the lattice of CeO₂ significantly enhances the concentration of OVs. However, interestingly, the relative concentration of OVs on CeO₂-r and Ce₁₀Sn₁O_x-r are smaller than those on CeO₂-c and Ce₁₀Sn₁O_x-c, respectively, suggesting that the concentration of OVs on the catalyst is not the only factor affecting the catalytic performance.

Surface electronic status information can be ascertained from UV-vis DRS measurement, as shown in Fig. 2d. All catalysts display three adsorption bands at ca. 208, 278, and 357 nm, the former band is probably related to the coordination state of tin species and the latter two bands are attributed to the charge-transfer of O²⁻ → Ce⁴⁺ and interband transitions, respectively [4,39,40]. Furthermore, the adsorption edges of Ce₁₀Sn₁O_x-r and Ce₁₀Sn₁O_x-c are shifted in the lower wavelength direction compared to CeO₂-r and CeO₂-c, implying that Sn⁴⁺ is incorporated into the lattice of CeO₂ to form composite oxide, thus causing a reduction in the symmetry and the development of strain on the sites of cerium [4,40], in agreement with XRD and Raman results. In addition, the adsorption band of SnO₂ is not detected and the broadening and/or weakening of the adsorption bands on Ce₁₀Sn₁O_x-r and Ce₁₀Sn₁O_x-c are also not obviously observed relative to those on CeO₂-r and CeO₂-c, suggesting that the doping of SnO₂ still retains the relatively complete structure of CeO₂.

TEM, HRTEM, and EDS mapping images were conducted on all the

catalysts to investigate their morphology, crystallite growth and elements distribution, as shown in Fig. 3. Both CeO₂-r and Ce₁₀Sn₁O_x-r nanorods display a narrow diameter distribution of 11–14 ± 2 nm, (Fig. 3a-d), both CeO₂-c and Ce₁₀Sn₁O_x-c nanocubes have a side length of between 14 and 30 nm (Fig. 3e-h), in accordance with the crystallite sizes determined by XRD. Moreover, the estimated d-spacings are ca. 0.32 and 0.31 nm in CeO₂-r and Ce₁₀Sn₁O_x-r, respectively, which are assigned to {1 1 1} plane of CeO₂ [41]. Similarly, the estimated d-spacings observed in CeO₂-c and Ce₁₀Sn₁O_x-c are ca. 0.27 and 0.26 nm, respectively, which are attributed to {1 0 0} plane of CeO₂ [26]. Meanwhile, {1 1 1} plane is also observed in ceria nanocubes, in agreement with the findings by Dai et al. [42]. Interestingly, the estimated d-spacings in Ce₁₀Sn₁O_x are a little smaller than those in CeO₂, suggesting that the doping of Sn⁴⁺ results in the shrinkage of unit cell, in consistent with the XRD results. In addition, the EDS mapping results indicate that Sn⁴⁺ is well-doped into CeO₂ (Fig. 3i-j).

3.3. Synergism between CeO₂ and SnO₂ as well as the bulk and surface compositions of CeO₂–SnO₂ catalysts

H₂-TPR results (Fig. 4a) were conducted to investigate the reducibility of CeO₂–SnO₂ catalysts. The peaks at ca. 447 and 471 °C for CeO₂-r and CeO₂-c are ascribed to the reduction of surface oxygen of CeO₂ [4]. It is obvious that CeO₂-r exhibits much lower reduction temperature and more H₂ consumption (Table S4) than CeO₂-c, suggesting that the reduction ability of CeO₂-r is much better than that of CeO₂-c, in consistent with their catalytic performance. Interestingly, when Sn⁴⁺ is incorporated into the lattice of CeO₂, the reduction temperatures of Ce₁₀Sn₁O_x-r and Ce₁₀Sn₁O_x-c are greatly reduced, and their experimental amounts of H₂ consumption (Table S4) are significantly increased and much higher than their estimated amounts, compared to CeO₂-r and CeO₂-c, respectively. Nevertheless, SnO₂ is almost inert in the temperature range. These facts indicate that the incorporation of

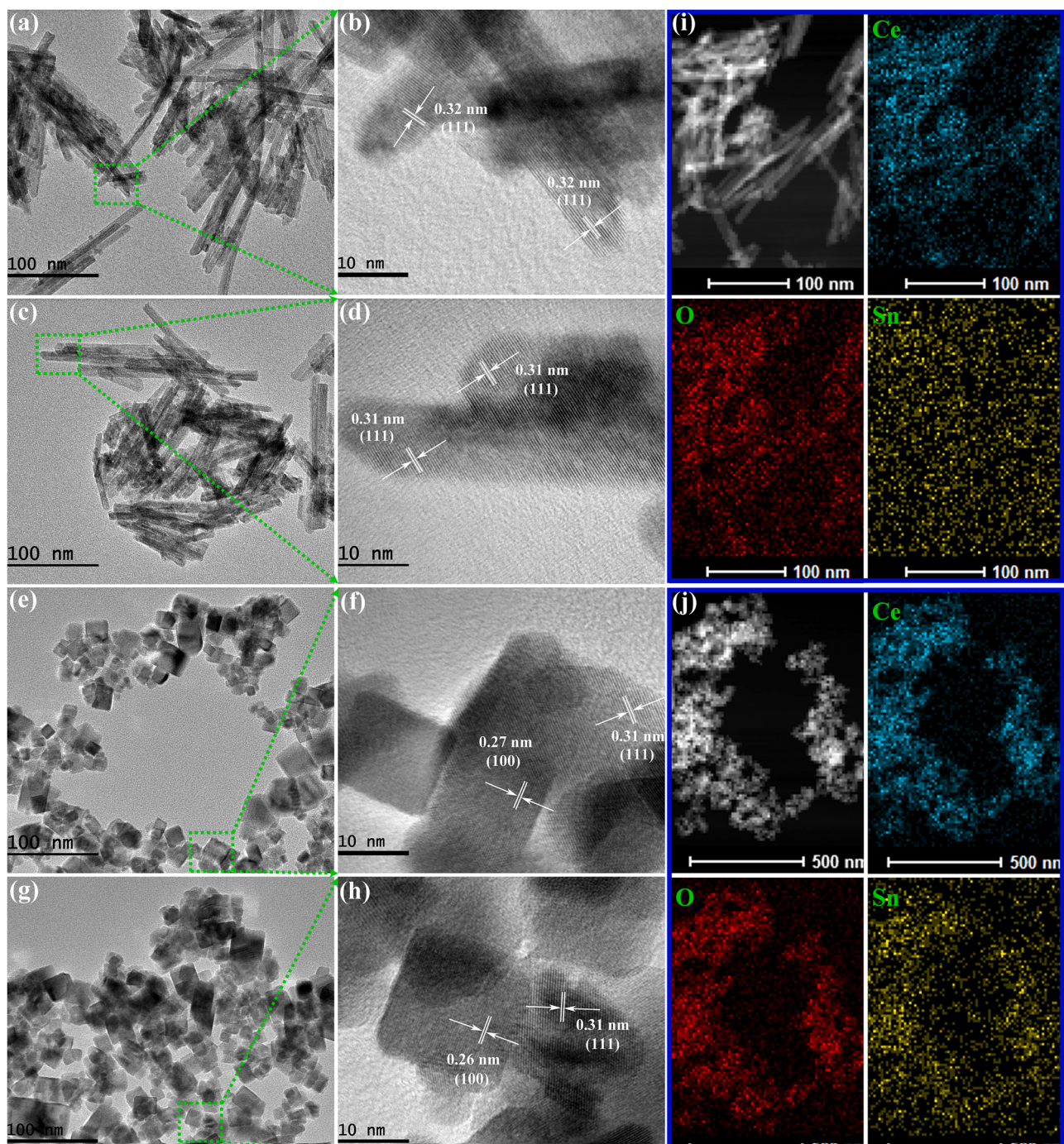


Fig. 3. The TEM, HRTEM, and EDS mapping images of CeO₂-r (a and b), Ce₁₀Sn₁O_x-r (c, d, and i), CeO₂-c (e and f), and Ce₁₀Sn₁O_x-c (g, h, and j).

Sn⁴⁺ significantly enhances the reducibility of CeO₂–SnO₂ catalysts and the elimination of the surface oxygen atoms results in the generation of vacancies. Then, the oxygen atoms in the bulk phase will migrate to the surface, whereas the vacancies will shift in the opposite direction [4]. According to the Raman and following EPR results, the doping of tin enhances the amount of defects and oxygen mobility in the lattice, very conducive to the reduction of CeO₂. Among which, Ce₁₀Sn₁O_x-r exhibits the best reduction ability.

CO₂-TPD results were carried out to investigate the interaction of product CO₂ on these typical catalysts in comparison, as shown in Fig. 4b. According to the literatures [43,44], the desorption of adsorbed CO₂ on the catalyst can be assigned to three types of characteristic peaks, i.e., molecularly adsorbed CO₂ (75–180 °C, weak basic site), HCO₃[−] or

HCO₃[−] (180–380 °C, medium basic site), as well as bidentate carbonates (b-CO₃^{2−}) and monodentate carbonates (m-CO₃^{2−}) (380–550 and 550–760 °C, respectively, strong basic sites). It is obvious that nanorod catalysts (They contain a large number of weak basic sites and a small number of medium basic sites) display much more desorption amount of CO₂ than those on cube catalysts (They contain weak, medium, and strong basic sites), implying that nanorod catalysts have more active sites compared to cube catalysts, in accordance with their catalytic performance. Moreover, for nanorod catalysts, Ce₁₀Sn₁O_x-r exhibits lower desorption temperature and less desorption amount of CO₂ than CeO₂-r, suggesting that the incorporation of Sn⁴⁺ into the lattice of CeO₂ can reduce the alkalinity of the catalysts and promote the desorption of CO₂, thus accelerating the reaction rate in both CO oxidation and NO

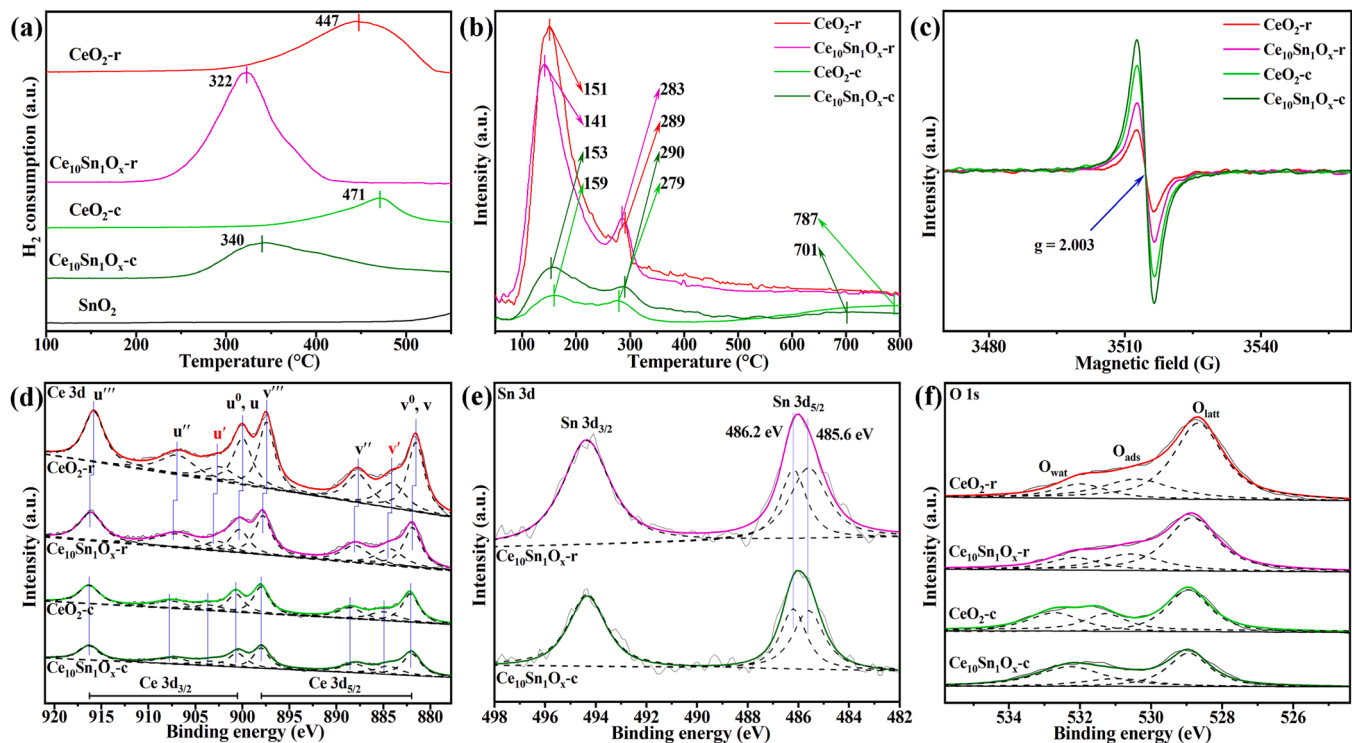
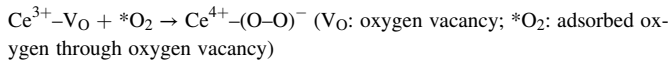


Fig. 4. (a) H₂-TPR results, (b) CO₂-TPD results, (c) EPR spectra, and XPS results of (d) Ce 3d, (e) Sn 3d, and (f) O 1 s of typical catalysts.

+ CO reaction. However, for cube catalysts, there exist obvious strong basic sites on the catalysts, which hinders the desorption of product CO₂ and leads to reduced reaction activities. EPR spectra (Fig. 4c) were performed to further investigate the signals of paramagnetic species caused by defects. A strong signal with g-factor of ca. 2.003 can be observed, which is attributed to O₂[−] superoxide ion formed by adsorption of oxygen through oxygen vacancy as following equation [45,46]:



After the incorporation of Sn⁴⁺ into the lattice of CeO₂, the concentrations of O₂[−] superoxide ion (or Ce³⁺) increase in both Ce₁₀Sn₁O_x-r and Ce₁₀Sn₁O_x-c, demonstrating that the incorporation of Sn⁴⁺ can enhance the concentration of OVs. In addition, it is obvious that the concentrations of OVs on CeO₂-r and Ce₁₀Sn₁O_x-r are less than those on CeO₂-c and Ce₁₀Sn₁O_x-c, respectively. These facts are well in agreement with Raman results.

The bulk compositions of these typical catalysts determined by ICP-AES and listed in Table S5 indicate that both the actual content of incorporated Sn⁴⁺ are slightly lower than the theoretical values. XPS measurement was conducted to unveil the surface chemical states of these typical catalysts. For Ce 3d XPS (Fig. 4d), all the spectra were fitted with eight components with assignments. The bands represented as v and u are ascribed to Ce 3d_{5/2} and Ce 3d_{3/2}, respectively. Furthermore, the bands labeled as v' and u' are related to Ce³⁺ and the rest six bands refer to Ce⁴⁺ [25]. The relative content of surface Ce³⁺ for all catalysts can be calculated by the following equation [19]:

$$\text{Ce}^{3+}(\%) = \frac{S_v + S_{v'}}{\sum(S_v + S_u)} \times 100\% \quad (S_v \text{ and } S_u \text{ are the areas of the bands labeled as v and u, respectively})$$

The relative contents of Ce³⁺ listed in Table S6 demonstrate that the incorporation of Sn⁴⁺ enhances the concentration of Ce³⁺ on Ce₁₀Sn₁O_x-r and Ce₁₀Sn₁O_x-c, compared to CeO₂-r and CeO₂-c. According to Raman and EPR results, the doping of Sn⁴⁺ enhances the amount of OVs. Furthermore, for ceria-based materials, the appearance of Ce³⁺ is

generally accompanied by the production of surface OVs [25,47]. In addition, the binding energy of Ce 3d on Ce₁₀Sn₁O_x-r shifts to a higher direction compared to CeO₂-r, but it is not obvious between CeO₂-c and Ce₁₀Sn₁O_x-c. These facts indicate that there exists strong synergism between CeO₂ and SnO₂, especially for Ce₁₀Sn₁O_x-r.

For Sn 3d XPS (Fig. 4e), both the Sn 3d_{5/2} bands in Ce₁₀Sn₁O_x-r and Ce₁₀Sn₁O_x-c can be deconvoluted into two bands at ca. 485.6 and 486.2 eV, attributed to Sn²⁺ and Sn⁴⁺, respectively [23]. As shown in Fig. 4e and Table S6, both the ratio of Sn²⁺ exceeds 50%, which is very consistent with the characteristics that SnO₂ is easy to produce defects and OVs [21,22]. Furthermore, the surface atomic concentration of Sn is more than that of bulk phase (Table S5 and S6), indicating that the surface doping ratio of Sn⁴⁺ is larger than that of bulk phase doping. This is one of the reasons for the increase of OVs on the surface of catalyst when Sn⁴⁺ is doped into CeO₂.

For O 1 s XPS (Fig. 4f), all the spectra were fitted with three bands at ca. 528.9, 530.5, and 532.2 eV, attributed to the lattice oxygen (O_{latt}), chemisorbed oxygen (O_{ads}), and surface oxygen from hydroxyl species and/or adsorbed water species on catalyst surface (O_{wat}) [10,48], respectively. As listed in Table S6 that the ratios of O_{ads} calculated based on the area ratio of O_{ads}/(O_{ads} + O_{latt}) in Ce₁₀Sn₁O_x are higher than those in pure CeO₂, implying that the doping of Sn⁴⁺ is conducive to the production of OVs. In addition, for all catalysts, the O/(Ce + Sn) ratios are much higher than the nominal ratio with their full oxidation state, and the superfluous surface oxygen may be related to the adsorption layer of CO₂, CO, or water with high concentration [1,49]. Trovarelli et al. had also reported that both CO and CO₂ are preferably adsorbed on Ce³⁺ sites to form carbonate-like species rather than on Ce⁴⁺ sites [50]. These facts indicate that the doping of Sn⁴⁺ enhances the concentration of OVs, thus increasing the ratio of reduced Ce³⁺ sites.

3.4. Identification of Sn species on CeO₂–SnO₂ catalysts

As described above, the doping of Sn⁴⁺ into CeO₂ can significantly tune the electronic structure toward excellent catalytic performances. Therefore, the structure of Sn, including the oxidation states as well as

local coordination environment, in the CeO_2 crystal is necessary to be well clarified. And XAS analysis was carried out for $\text{Ce}_{10}\text{Sn}_1\text{O}_x\text{-r}$ and $\text{Ce}_{10}\text{Sn}_1\text{O}_x\text{-c}$ and shown in Fig. 5. It can be found that the positions of the peaks of $\text{Ce}_{10}\text{Sn}_1\text{O}_x\text{-r}$ and $\text{Ce}_{10}\text{Sn}_1\text{O}_x\text{-c}$ are between SnO and SnO_2 but closer to SnO_2 , indicating that the Sn species in both $\text{Ce}_{10}\text{Sn}_1\text{O}_x\text{-r}$ and $\text{Ce}_{10}\text{Sn}_1\text{O}_x\text{-c}$ are mainly in the form of Sn^{4+} and contain a small number of Sn^{2+} , in consistent with the XPS and XANES fitting results (Fig. 4e and Table S7). As shown in the EXAFS results in R space, the peaks at ca. 1–2 and 2.5–4 Å are ascribed to the $\text{Sn}-\text{O}$ and $\text{Sn}-\text{Sn}$ bonds, respectively [51]. Moreover, the absence of $\text{Sn}-\text{Sn}$ coordination shell and the presence of exclusive $\text{Sn}-\text{O}$ coordination environment (Fig. 5b and Table S7) in $\text{Ce}_{10}\text{Sn}_1\text{O}_x\text{-r}$ and $\text{Ce}_{10}\text{Sn}_1\text{O}_x\text{-c}$ indicate that the Sn species in both catalysts almost exist in the form of single-site [52]. According to these data for curve fitting, it is difficult to clearly identify and distinguish the $\text{Ce}-\text{O}-\text{Sn}$ bond by reason of the very low intensity of presumable coordination shells in R space (>2 Å) for Sn K-edge EXAFS. However, the bond lengths ascribed to the $\text{Sn}-\text{O}$ bond in $\text{Ce}_{10}\text{Sn}_1\text{O}_x\text{-r}$ and $\text{Ce}_{10}\text{Sn}_1\text{O}_x\text{-c}$ slightly shift compared to that in SnO_2 , which may be caused by the influence of Ce in $\text{Ce}-\text{O}-\text{Sn}$ bond.

3.5. Reaction mechanism

3.5.1. CO and/or O_2 interaction with typical catalysts

To investigate the interaction between CO and O_2 during the reaction as well as the reaction mechanism on the catalysts, systematic in situ DRIFTS experiments were collected as shown in Fig. 6. Firstly, in CO adsorption experiment, it is obvious that multiple adsorption peaks appear on $\text{Ce}_{10}\text{Sn}_1\text{O}_x\text{-r}$ (Fig. 6a) at a lower temperature. The peaks at ca. 1036, 1285, and 1536 cm^{-1} are generally attributed to the different vibrations of monodentate carbonates ($\nu(\text{C}-\text{O})$, $\nu_s(\text{CO}_3^{2-})$, and $\nu_{as}(\text{CO}_3^{2-})$), respectively; the peak at ca. 1216 cm^{-1} refers to the vibration of hydrogencarbonates ($\delta(\text{C}-\text{O}-\text{H})$); the peaks at ca. 1399 and 1585 cm^{-1} are ascribed to the vibrations of carboxylates ($\nu_s(\text{COO}^-)$ and $\nu_{as}(\text{COO}^-)$), respectively; the peak at ca. 1639 cm^{-1} is attributed to the vibration of bidentate bicarbonate [1,4,19,23]. Furthermore, the peak at ca. 1036 cm^{-1} disappears when the temperature increase to 175 °C and a new peak attributed to the vibration of CO_x on Ce^{3+} appears at ca. 1070 cm^{-1} at the same temperature, demonstrating that $\text{Ce}_{10}\text{Sn}_1\text{O}_x\text{-r}$ can be reduced by CO at a certain temperature [53]. According to the literatures [23,50], CO and CO_2 are preferably adsorbed on Ce^{3+} sites to form carbonate-like species rather than on oxidized Ce^{4+} sites. Therefore, the increase of the intensities in these carbonates and carboxylates with increasing temperature indicates that an increasing number of Ce^{4+} are reduced to Ce^{3+} with the increase of temperature during CO atmosphere. And at higher temperature, there appear obvious characteristic peaks of gaseous CO and CO_2 at ca. 2113–2178 and 2362 cm^{-1} . In

addition, except for two points, CO adsorption on $\text{Ce}_{10}\text{Sn}_1\text{O}_x\text{-c}$ (Fig. 6c) is very similar to that on $\text{Ce}_{10}\text{Sn}_1\text{O}_x\text{-r}$. One is that two new peaks ascribed to carbonates and/or carboxylates appear at ca. 1330 and 1470 cm^{-1} , which may be originated from the inherent difference of surface structure between $\text{Ce}_{10}\text{Sn}_1\text{O}_x\text{-c}$ and $\text{Ce}_{10}\text{Sn}_1\text{O}_x\text{-r}$. The other is that the strength of adsorbed species of CO on $\text{Ce}_{10}\text{Sn}_1\text{O}_x\text{-c}$ is much smaller than that of $\text{Ce}_{10}\text{Sn}_1\text{O}_x\text{-r}$, suggesting that the reducibility of $\text{Ce}_{10}\text{Sn}_1\text{O}_x\text{-r}$ is much stronger than that of $\text{Ce}_{10}\text{Sn}_1\text{O}_x\text{-c}$, in agreement with H₂-TPR results.

Secondly, in CO and O_2 coadsorption experiment, the peaks of carbonates, carboxylates, and hydrogencarbonates also appear on $\text{Ce}_{10}\text{Sn}_1\text{O}_x\text{-r}$ (Fig. 6b) at a lower temperature. But obviously, the intensities of these peaks in CO and O_2 atmosphere are much weaker than those in single CO atmosphere at the same temperature, indicating that O_2 molecules are preferentially adsorbed on the catalyst surface and occupy the surface OVs, thus hindering the adsorption of CO [1]. Another point must be noted is that the intensity of the peak attributed to the vibration of CO_x on Ce^{3+} in CO and O_2 atmosphere becomes much weaker than that in single CO atmosphere after 150 °C, suggesting that excess O_2 makes it difficult to reduce Ce^{4+} to Ce^{3+} . After gradually increasing the temperature, the intensities of these peaks in CO and O_2 atmosphere are still much weaker than those in single CO atmosphere. One is that the surface content of Ce^{3+} decreases, resulting in the reduction of CO adsorption sites; the other is that the reaction of the adsorbed CO with the adsorbed O_2 species, formed by the adsorption of O_2 on the surface OVs, to CO_2 . Equally, the evolution of adsorbed species on the surface of $\text{Ce}_{10}\text{Sn}_1\text{O}_x\text{-c}$ (Fig. 6d) in CO and O_2 atmosphere is similar to that of $\text{Ce}_{10}\text{Sn}_1\text{O}_x\text{-r}$.

3.5.2. CO and/or NO interaction with typical catalysts

In NO + CO reaction, the oxidation of CO is one of the two half-reactions, which is identical with CO oxidation in CO + O_2 reaction. Therefore, for the adsorption of single CO, the evolution of adsorbed species on the catalyst surface in NO + CO reaction is very similar to that in CO oxidation (Fig. 6). On the other hand, in NO adsorption experiment, it is obvious that multiple adsorption peaks appear on $\text{Ce}_{10}\text{Sn}_1\text{O}_x\text{-r}$ (Fig. 7a) at a lower temperature. The peaks at ca. 1040 and 1607 cm^{-1} are assigned to the different vibrations of bridging bidentate nitrate; the peak at ca. 1237 cm^{-1} is ascribed to the asymmetric vibration of linear nitrite; the two peaks at ca. 1280 and 1509 cm^{-1} are attributed to the vibrations of monodentate nitrate; the peaks at ca. 1355 and 1569 cm^{-1} are assigned to the vibrations of hyponitrites (NO^-) and bridging monodentate nitrate, respectively [4,19,31,54,55]. Moreover, the intensities of these monodentate and bidentate nitrates and linear nitrite decrease gradually with increasing temperature and the peak at ca. 1280 cm^{-1} disappears after 200 °C. On the contrary, two new peaks

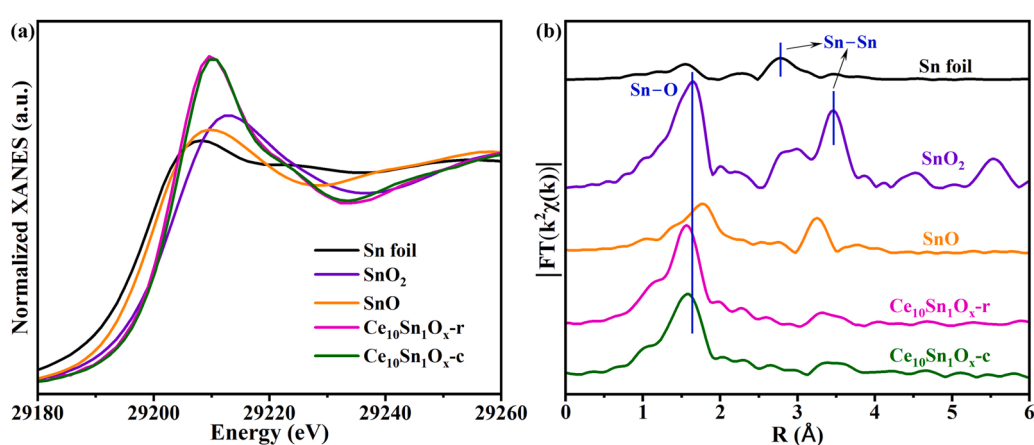


Fig. 5. Normalized XANES (a) and EXAFS (b) spectra of Fourier transformed k^2 -weighted $\chi(k)$ at Sn-K edge for $\text{Ce}_{10}\text{Sn}_1\text{O}_x\text{-r}$ and $\text{Ce}_{10}\text{Sn}_1\text{O}_x\text{-c}$. Sn foil, SnO_2 , and SnO were used as references.

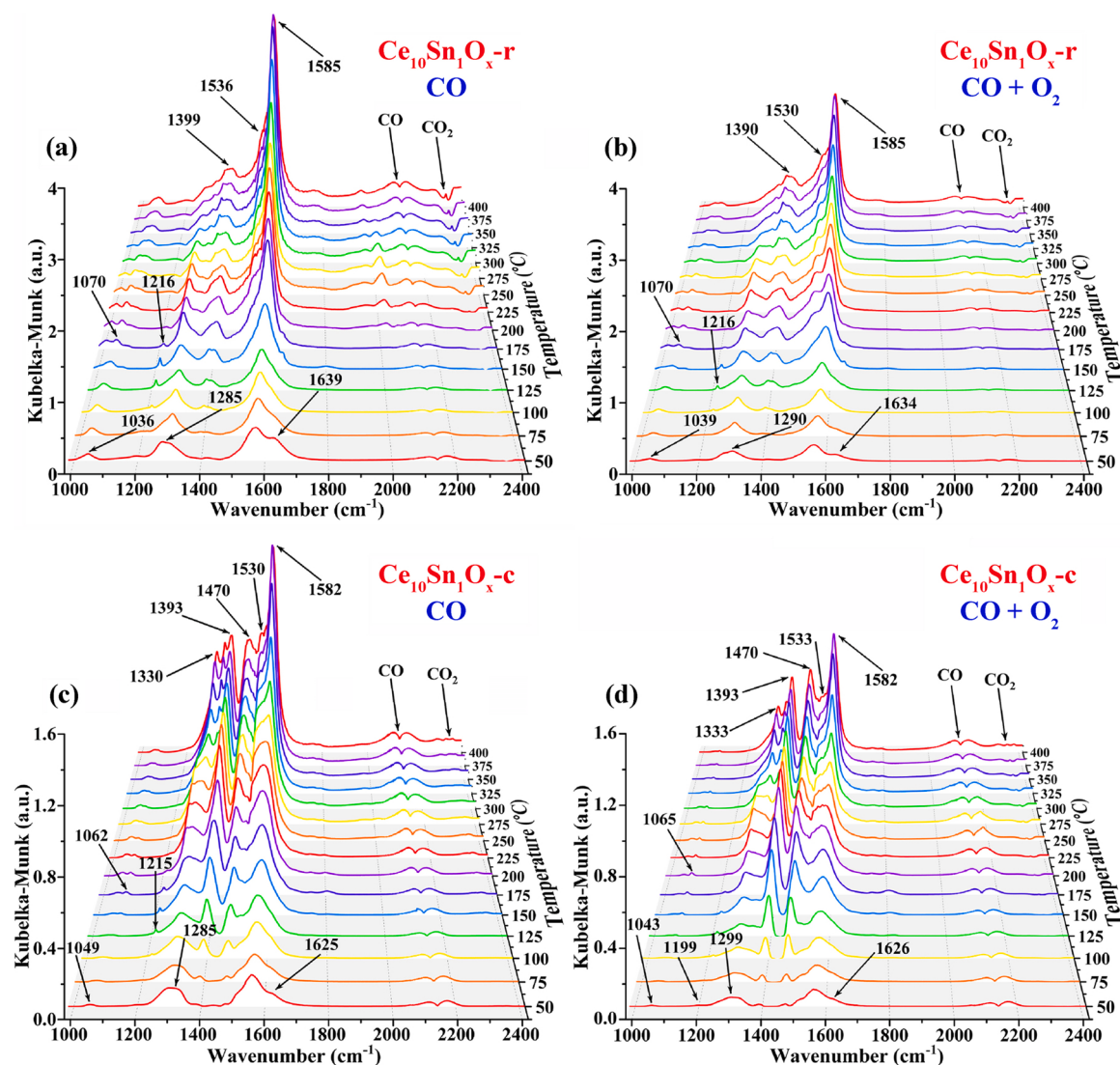


Fig. 6. *In situ* DRIFTS spectra of CO (10 vol% CO/Ar) adsorption on Ce₁₀Sn₁O_x-r (a) and Ce₁₀Sn₁O_x-c (c), and CO (10 vol% CO/Ar) and O₂ (20 vol% O₂/Ar) coadsorption on Ce₁₀Sn₁O_x-r (b) and Ce₁₀Sn₁O_x-c (d).

ascribed to the vibrations of chelating bidentate nitrate appear at ca. 1203 and 1541 cm⁻¹ after 200 °C. These facts indicate that the adsorbed NO species undergo rearrangement rather than complete desorption or decomposition during the process of continuous warming [56]. In addition, NO adsorption on Ce₁₀Sn₁O_x-c (Fig. 7c) is very similar to that on Ce₁₀Sn₁O_x-r. However, the intensity weakening of NO species on Ce₁₀Sn₁O_x-r is significantly stronger than that on Ce₁₀Sn₁O_x-c after increasing the temperature, suggesting that the adsorbed NO species on Ce₁₀Sn₁O_x-r surface are easier to desorb/transform/decompose than those on Ce₁₀Sn₁O_x-c surface [4]. Another point must be noted is that the formation of NO⁻ is due to the electron transfer from a reduced Ce³⁺ to a NO molecule at the interfacial sites of OVs [55], the NO⁻ species can be easily dimerized into N₂O₂⁻ and further decomposed into N₂O at low temperatures [19].

To further explore the reaction mechanism on the catalysts, CO and NO coadsorption on the catalysts was carried out as shown in Fig. 7b and d. Obviously, the peaks of nitrite-/nitrate-like species can be observed on Ce₁₀Sn₁O_x-r (Fig. 7b) below 275 °C, but that of carbonates, carboxylates, and hydrogencarbonates can not be observed in this temperature range, indicating that NO molecules are preferentially adsorbed on the catalyst owing to its unpaired electron, thus hindering the adsorption of CO [1,19]. When the temperature exceeds 275 °C, the adsorbed NO

species disappear due to desorb/transform/decompose/reaction. Instead, CO adsorption can be obviously observed on the active sites (Ce³⁺ and/or Sn²⁺) [23]. In addition, CO and NO coadsorption on Ce₁₀Sn₁O_x-c (Fig. 7d) is also very similar to that on Ce₁₀Sn₁O_x-r. However, the adsorption strengths of NO and CO on Ce₁₀Sn₁O_x-r are much higher than those on Ce₁₀Sn₁O_x-c. The former is due to more quantity or faster formation rate of OVs during heating, the latter is due to more Ce³⁺ during reduction. Moreover, more gaseous CO and CO₂ on Ce₁₀Sn₁O_x-r than those on Ce₁₀Sn₁O_x-c further suggest that the reaction rate of NO + CO on Ce₁₀Sn₁O_x-r is much faster than that on Ce₁₀Sn₁O_x-c.

3.5.3. DFT calculations

Both CO oxidation and NO + CO reaction are closely related to the adsorption and desorption of reactants and products as well as the OVs on the catalyst surface. Therefore, DFT calculations were conducted to further understand the mechanisms, including the effect of the incorporation of Sn⁴⁺ on the formation energy of OVs and the potential energies during the reactions at the atomic level.

It is generally believed that OVs are the adsorption and activation sites of O₂ in CO oxidation and of NO in NO + CO reaction [1,25,57,58]. As discussed above, the incorporation of Sn⁴⁺ into CeO₂ can result in the formation of OVs. In addition, according to the TEM results (Fig. 3), the

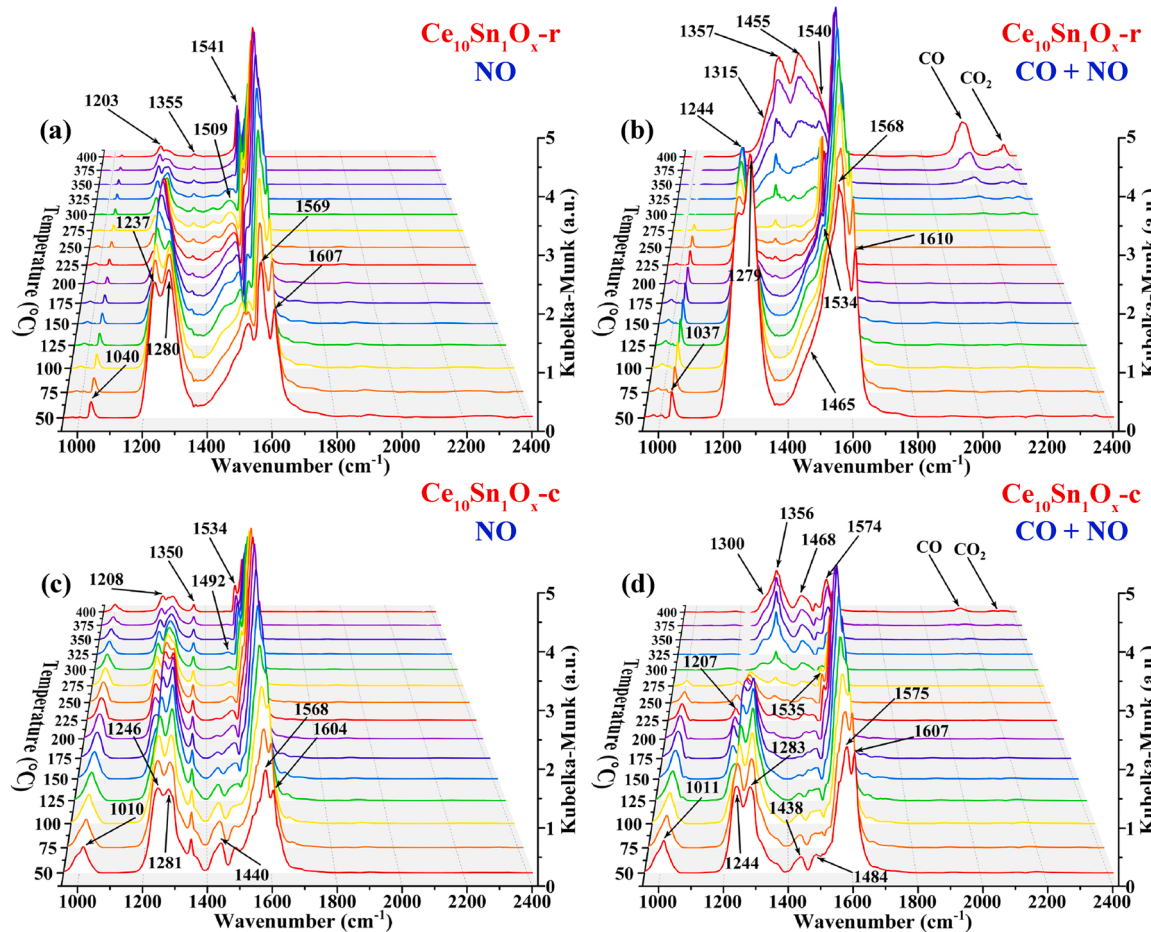


Fig. 7. *In situ* DRIFTS spectra of NO (5 vol% NO/Ar) adsorption on $\text{Ce}_{10}\text{Sn}_1\text{O}_x\text{-r}$ (a) and $\text{Ce}_{10}\text{Sn}_1\text{O}_x\text{-c}$ (c), and CO (10 vol% CO/Ar) and NO (5 vol% NO/Ar) coadsorption on $\text{Ce}_{10}\text{Sn}_1\text{O}_x\text{-r}$ (b) and $\text{Ce}_{10}\text{Sn}_1\text{O}_x\text{-c}$ (d).

nanorods mainly expose {1 1 1} facet and the nanocubes expose {1 1 1} and {1 0 0} facets at the same time. Therefore, two slabs with the perfect {1 1 1} facet of CeO_2 (labeled as CeO_2) and {1 1 1} facet of Sn^{4+} doped CeO_2 (labeled as $\text{Ce}_{10}\text{Sn}_1\text{O}_x$) were built and optimized as shown in Fig. 8. For CeO_2 , the formation energy of OVs (ΔE_{OV}) on the surface and subsurface are 2.37 and 4.40 eV, respectively, similar to the results reported by Tian et al. [9]. After doping Sn^{4+} , the ΔE_{OV} on the surface and subsurface reduce to 0.69 and 3.12 eV, respectively. Herein two conclusions can be obtained. Firstly, the doping of Sn^{4+} , no matter the surface and subsurface, can greatly reduce the ΔE_{OV} , indicating that the doped Sn^{4+} can activate the oxygen atoms near the Sn atom, thus promoting the formation of OVs. Secondly, both the ΔE_{OV} on the surface are lower than those on subsurface whether it is CeO_2 or $\text{Ce}_{10}\text{Sn}_1\text{O}_x$, suggesting that the doping of Sn^{4+} is more conducive to the generation of surface OVs. In addition, the much lower ΔE_{OV} over $\text{Ce}_{10}\text{Sn}_1\text{O}_x$ are also consistent with the much more OVs over $\text{Ce}_{10}\text{Sn}_1\text{O}_x\text{-r}$ and $\text{Ce}_{10}\text{Sn}_1\text{O}_x\text{-c}$ determined by Raman, EPR, and XPS results.

To have a better understanding of the reaction mechanism on the catalysts, the potential energies were performed by DFT calculations, as shown in Fig. 9. For CO oxidation (Fig. 9a), *in situ* DRIFTS results (Fig. 6) suggest that CO is mainly adsorbed on reduced Ce^{3+} (and/or Sn^{2+}) and O_2 can be activated into O_2^- species on OVs. Therefore, the active site should contain the oxygen vacancy and its adjacent unsaturated Ce and Sn shown in Fig. S6. It is obvious that the adsorptions of CO and O_2 are spontaneous and the incorporation of Sn^{4+} is more conducive to the adsorptions of the two reactants. Then the reaction between adsorbed CO and O_2^- species is a strong endothermic process, a + 4.26 eV energy input is needed to drive this process on CeO_2 , but only + 3.21 eV energy

can drive this process on $\text{Ce}_{10}\text{Sn}_1\text{O}_x$. The transition state structure TS1 is shown in Fig. S6. At the same time, this step is also a rate-determining step. Then, the production of adsorbed CO_2 on the catalysts is also spontaneous. The last step, namely, the desorption of CO_2 becomes an endothermic process due to the weak alkalinity of CeO_2 , however, the energy barrier to be overcome on $\text{Ce}_{10}\text{Sn}_1\text{O}_x$ (+ 3.13 eV) is still lower than that on CeO_2 (+ 3.49 eV). These results above demonstrate that the doping of Sn^{4+} into CeO_2 can rearrange the electronic structure around the oxygen vacancy and its adjacent unsaturated Ce and Sn, further activate the adsorbed CO and O_2^- species, and weaken the interaction between the active site and CO_2 that is in agreement with the CO₂-TPD results, thus greatly increasing the reaction rate of CO oxidation. In addition, the reaction transition states of the reaction on the two catalysts are shown in Fig. S6.

For NO + CO reaction (Fig. 9b), according to previous reports [1,4, 23,31,54,57] and *in situ* DRIFTS results (Fig. 7), CO is mainly adsorbed on reduced Ce^{3+} (and/or Sn^{2+}) and NO can be activated into N and O species on OVs. Therefore, the active site should also contain the oxygen vacancy and its adjacent unsaturated Ce and Sn shown in Fig. S7. Similarly, the adsorptions of CO and NO are spontaneous and the doping of Sn^{4+} is more beneficial to the adsorptions of them. The next step is the dissociation of N – O bond on the OVs, a + 2.06 eV energy input is needed to drive this process on CeO_2 , but only + 1.60 eV energy can drive this process on $\text{Ce}_{10}\text{Sn}_1\text{O}_x$. The transition state structure TS1 is shown in Fig. S7. Then, the next step, a rate-determining step, contains the coupling of adsorbed CO and dissociated O as well as two dissociated N. Large energy barrier of + 5.04 eV needs to be overcome on CeO_2 , however, only + 3.80 eV energy can drive this process on $\text{Ce}_{10}\text{Sn}_1\text{O}_x$.

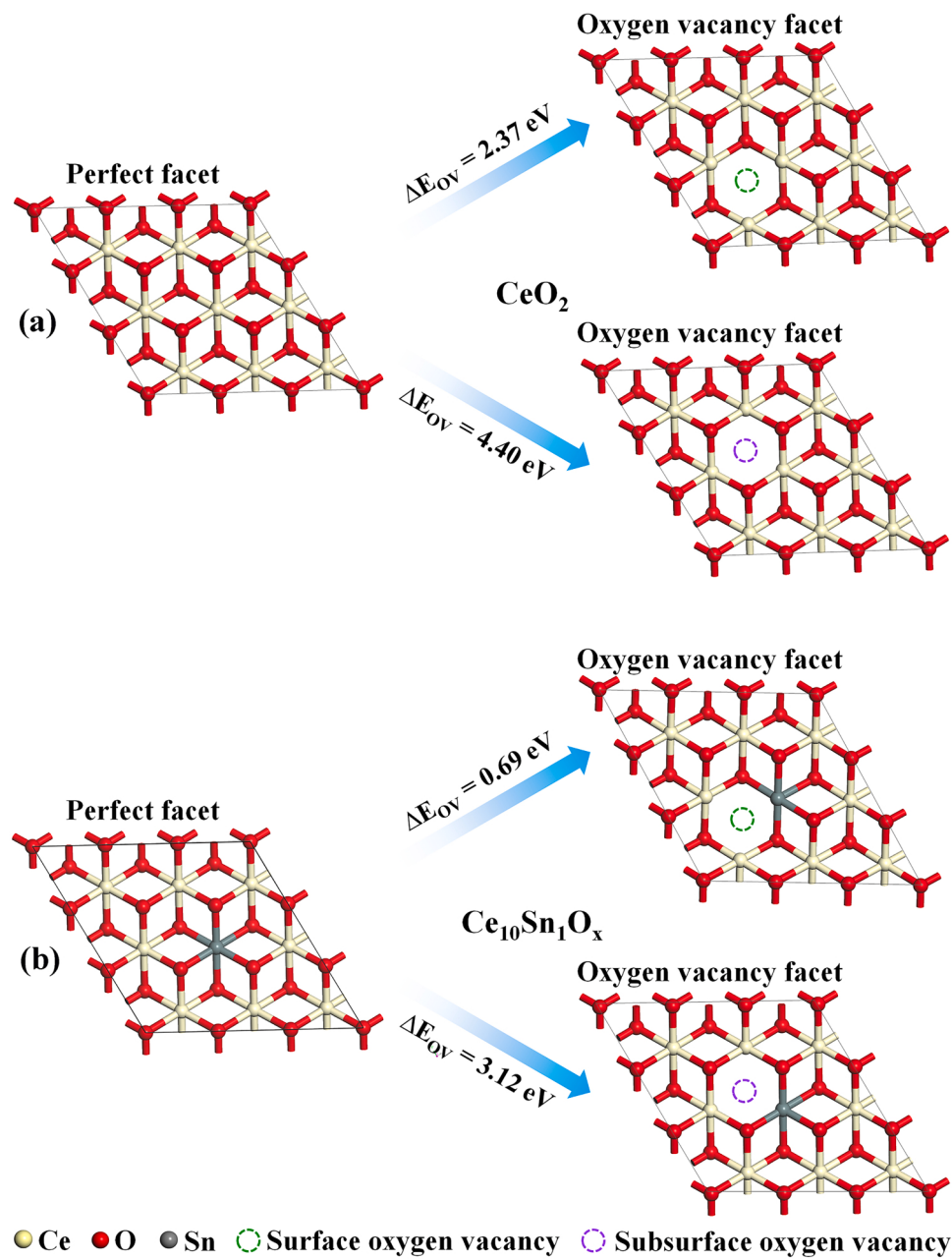


Fig. 8. Formation energy of a surface or subsurface oxygen vacancy over (a) CeO_2 and $\text{Ce}_{10}\text{Sn}_1\text{O}_x$ (b) (111, as an example).

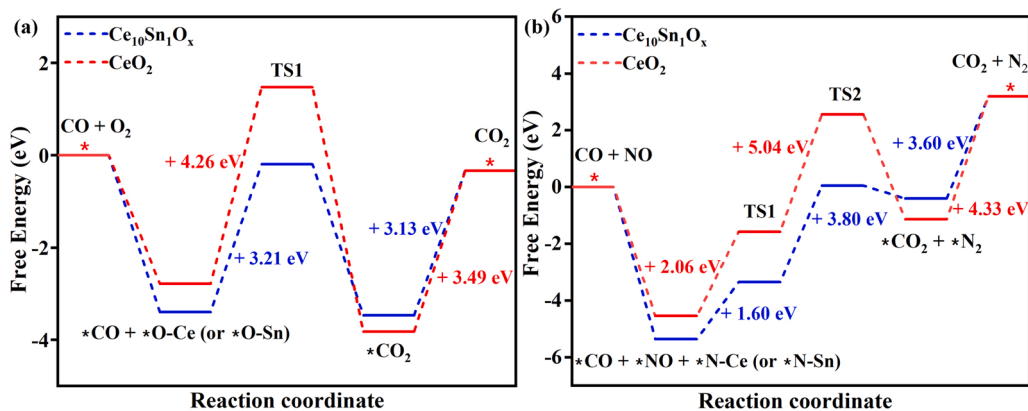


Fig. 9. Results of DFT calculations: potential energies of CeO_2 and $\text{Ce}_{10}\text{Sn}_1\text{O}_x$ over CO oxidation (a) and NO + CO reaction (b) (111, as an example).

The transition state structure TS2 is also shown in Fig. S7. In this step, the energy barrier contains the formation energy barrier of CO_2 and the recombination energy barrier of N_2 , but their specific contributions to the energy barrier are difficult to distinguish due to the close relationship in the two processes. In like wise, the formation of adsorbed CO_2 and N_2 is spontaneous. At last, the desorptions of CO_2 and N_2 are an endothermic process, the energy barrier to be overcome on $\text{Ce}_{10}\text{Sn}_1\text{O}_x$ (+ 3.60 eV) is still lower than that on CeO_2 (+ 4.33 eV). In addition, the reaction transition states of the reaction on the two catalysts are shown in Fig. S7. As discussed above, the doping of Sn^{4+} into CeO_2 can further activate the adsorbed CO and NO species, promote the dissociation of N – O bond as well as the coupling intermediate species, and weaken the interaction between the active site and products, thus significantly enhancing the reaction rate of $\text{NO} + \text{CO}$ reaction.

3.6. Active sites on $\text{CeO}_2-\text{SnO}_2$ catalysts for CO oxidation and $\text{NO} + \text{CO}$ reaction

As described in the above discussion of catalytic performances, the doping of Sn^{4+} into CeO_2 exhibits similar promotional effects on both CO oxidation and $\text{NO} + \text{CO}$ reaction whether it is the structures of nanorod or nanocube. These effects are mainly as follows: XRD, N_2 sorption, Raman, UV-vis DRS, and TEM results reveal that the doping of little Sn^{4+} into CeO_2 has an almost negligible effect on the main structure of CeO_2 . H_2 -TPR results disclose that the doping of Sn^{4+}

significantly enhances the mobility of lattice oxygen, thus increasing its reducibility. Moreover, Raman, EPR, and XPS results unlock that the concentrations of OV are greatly increased by the incorporation of Sn^{4+} . Meanwhile, the formation energies of OV are greatly reduced, according to the DFT calculation results. Therefore, the active sites on the catalysts should have commonality in CO oxidation and $\text{NO} + \text{CO}$ reaction.

In CO oxidation, as discussed in the in situ DRIFTS and DFT calculation results, CO is adsorbed on reduced Ce^{3+} (and/or Sn^{2+}), forming carbonates and carboxylates species, and O_2 is activated into O_2^- species on OV. Moreover, XAS results demonstrate that the Sn species in the catalysts almost exist in the form of single-site. Therefore, the crucial adsorption/active site should contain the oxygen vacancy and its adjacent unsaturated Ce and Sn (in a form of $\text{Sn}^{2+}-\text{O}_v-\text{Ce}^{3+}$). The doping of Sn^{4+} significantly enhances the adsorption quantity of these carbonates and carboxylates, implying that more OV are produced, which further supports the above structural style of adsorption/active site. In addition, there must exists adsorption/active site in a form of $\text{Ce}^{3+}-\text{O}_v-\text{Ce}^{3+}$ because the atomic concentration of Ce is about ten times that of Sn on the catalyst surface (Table S6). But the $\text{Sn}^{2+}-\text{O}_v-\text{Ce}^{3+}$ adsorption/active site plays a more critical role during catalysis compared to $\text{Ce}^{3+}-\text{O}_v-\text{Ce}^{3+}$. The schematic diagram of the adsorption/active site and possible mechanism on $\text{Ce}_{10}\text{Sn}_1\text{O}_x$ -r and $\text{Ce}_{10}\text{Sn}_1\text{O}_x$ -c catalysts are depicted as the left side of Fig. 10.

In $\text{NO} + \text{CO}$ reaction, as discussed in the in situ DRIFTS results, more

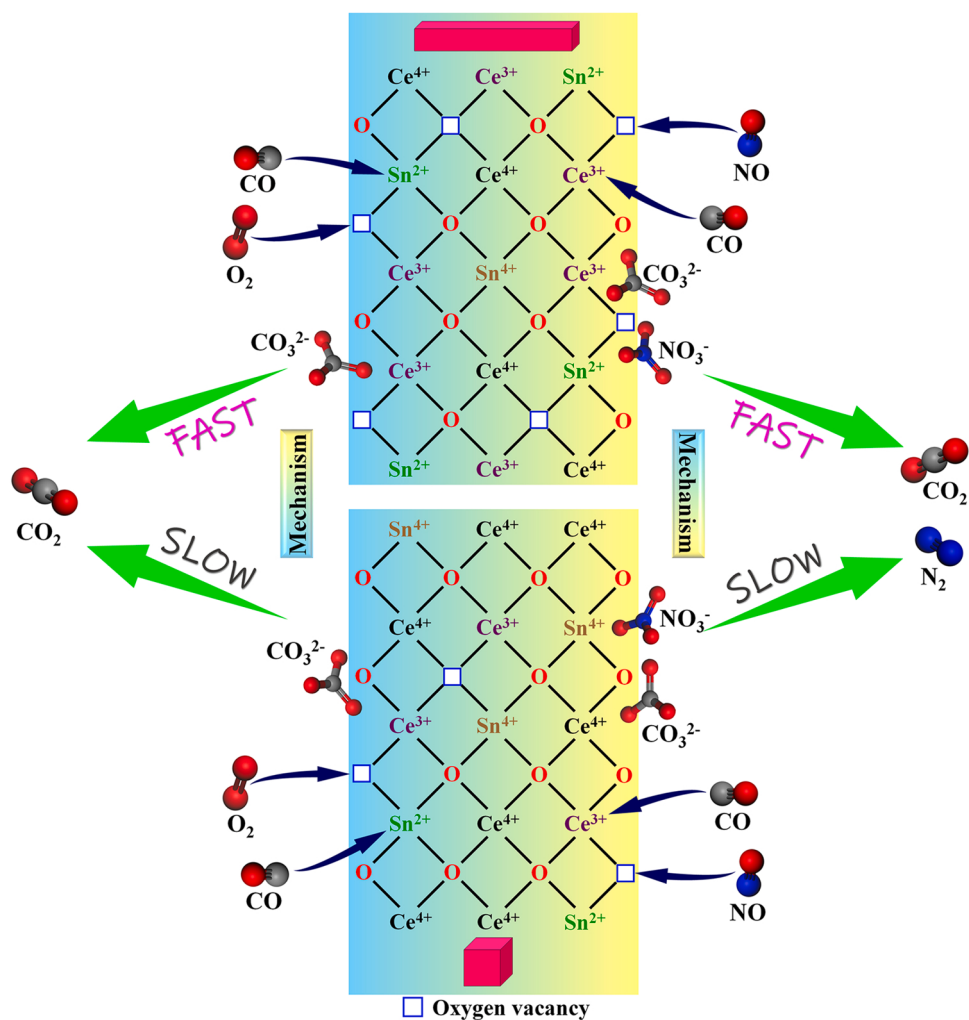


Fig. 10. Schematic of the possible reaction mechanisms for CO oxidation (Left) and $\text{NO} + \text{CO}$ reaction (Right) on the surface of $\text{Ce}_{10}\text{Sn}_1\text{O}_x$ -r and $\text{Ce}_{10}\text{Sn}_1\text{O}_x$ -c catalysts.

reactive monodentate and bidentate nitrates and linear nitrite are presented on $\text{Ce}_{10}\text{Sn}_1\text{O}_x\text{-r}$ compared to $\text{Ce}_{10}\text{Sn}_1\text{O}_x\text{-c}$, implying that the quantity of OVs on the former is more than that on the latter. Although Raman, EPR, and XPS results suggest that the concentration on $\text{Ce}_{10}\text{Sn}_1\text{O}_x\text{-r}$ is a little lower than that on $\text{Ce}_{10}\text{Sn}_1\text{O}_x\text{-c}$, the specific surface area of the former is nearly three times that of the latter. Therefore, the quantity of OVs on $\text{Ce}_{10}\text{Sn}_1\text{O}_x\text{-r}$ should much more than that on $\text{Ce}_{10}\text{Sn}_1\text{O}_x\text{-c}$. Previous studies had indicated that NO can be efficiently adsorbed and activated on the OVs to dissociate into [N] and [O] (active oxygen species) radicals [4,23,25]. For one of the two half-reactions, i.e., CO oxidation, the reaction between adsorbed CO species on Ce^{3+} (and/or Sn^{2+}) and active [O] species came from the dissociation of adsorbed NO is one of the most critical steps. Furthermore, it is obvious that the oxidation of adsorbed CO species on Ce^{3+} (and/or Sn^{2+}) is easy to be occurred at elevated temperatures (such as 250 °C). Consequently, the ease of the transfer of dissociated [O] to the Ce^{3+} (and/or Sn^{2+}) site should play a vital role in determining the removal efficiency of CO. And the doping of Sn^{4+} can make the transfer from dissociated [O] to the Ce^{3+} (and/or Sn^{2+}) site easier. On the other hand, the reaction temperatures in CO oxidation on the catalysts (such as $\text{Ce}_{10}\text{Sn}_1\text{O}_x\text{-r}$, $T_{50} = 218$ °C) are much lower than those in NO + CO reaction ($T_{50} = 265$ °C), also demonstrating that the dissociation rate of NO and the migration rate of dissociated [O] species to Ce^{3+} (and/or Sn^{2+}) site should be one of the key steps in the reaction. Combining with the above discussion, the efficient adsorption/active site can also be expressed in the form of $\text{Sn}^{2+}\text{-O}_v\text{-Ce}^{3+}$ [23]. The schematic diagram of the adsorption/active site and possible mechanism on $\text{Ce}_{10}\text{Sn}_1\text{O}_x\text{-r}$ and $\text{Ce}_{10}\text{Sn}_1\text{O}_x\text{-c}$ catalysts are described as the right side of Fig. 10.

According to these discussions, it can be concluded that CO oxidation and NO + CO reaction on Sn^{4+} doped CeO_2 catalysts (both nanorod and nanocube) share the same adsorption/active site, i.e., $\text{Sn}^{2+}\text{-O}_v\text{-Ce}^{3+}$, on which CO is adsorbed on reduced Ce^{3+} (and/or Sn^{2+}), O_2 and NO are adsorbed on the OVs. And the CO oxidation half-reaction should have obvious dependence on the active [O] species derived from the dissociation of NO species during NO + CO reaction. In addition, the doping of Sn^{4+} into CeO_2 can rearrange the electronic structure of $\text{Sn}^{2+}\text{-O}_v\text{-Ce}^{3+}$ site, further activate the adsorbed CO and O_2/NO species, and weaken the interaction between the active site and product CO_2 by reducing the alkalinity of the catalysts.

4. Conclusions

In summary, the doping of Sn^{4+} into CeO_2 exhibits greatly promotional effects on both CO oxidation and NO + CO reaction whether it is the structures of nanorod or nanocube, which benefits from the formation of more OVs, stronger redox ability that can enhance the mobility of lattice oxygen, lower formation energies of OVs, and weaker alkalinity that can increase the desorption of product CO_2 . Among which, the catalytic performances of $\text{Ce}_{10}\text{Sn}_1\text{O}_x\text{-r}$ are much more outstanding than that of $\text{Ce}_{10}\text{Sn}_1\text{O}_x\text{-c}$ due to the easier generation and implementation of the above positive factors. And the main structure of CeO_2 itself is proved to be well preserved. For both CO oxidation and NO + CO reaction, they share the same adsorption/active site, i.e., $\text{Sn}^{2+}\text{-O}_v\text{-Ce}^{3+}$ (main adsorption/active site) on Sn^{4+} doped CeO_2 catalysts. The unsaturated Ce^{3+} (and/or Sn^{2+}) under reaction conditions are the most active sites during CO adsorption and further oxidation; the OVs are the adsorption/active sites of O_2 and NO; and the rearrangement of the electronic structure on $\text{Sn}^{2+}\text{-O}_v\text{-Ce}^{3+}$ site can facilitate the dissociation of O_2 and NO as well as further transfer of dissociated [O] species to advance the formation of N_2 and depletion of CO. Meanwhile, the CO oxidation half-reaction has obvious dependence on the active [O] species derived from the dissociation of NO species during NO + CO reaction. The findings proposed in this work provide an uncomplicated but effective strategy for the design and synthesis of noble metals-free catalysts in vehicle emission control, flesh out the understanding of the construction of efficient cerium-based catalysts doped with foreign

elements utilizing shape supports, and is also a step forward in the understanding of CO oxidation and NO + CO reaction over $\text{CeO}_2\text{-SnO}_2$ catalysts.

CRediT authorship contribution statement

C. Deng: Conceptualization, Methodology, Investigation, Formal analysis, Writing – original draft, Writing – review & editing, Funding acquisition. **X. Qian:** Investigation. **T. Zhao:** Investigation. **M. Lu:** Methodology, Formal analysis. **Q. Liu:** Methodology, Formal analysis. **J. Yang:** Data curation. **T. Chen:** Project administration, Supervision, Conceptualization, Writing – review & editing, Funding acquisition. **L. Dong:** Project administration, Supervision, Conceptualization, Writing – review & editing, Funding acquisition.

Declaration of Competing Interest

The authors declare that they have no known competing financial interests or personal relationships that could have appeared to influence the work reported in this paper.

Data Availability

Data will be made available on request.

Acknowledgments

The authors thank the financial support from the National Science Foundation of China (22202101). The authors would like to thank Zhengjie Chen from SCI-GO (www.sci-go.com) for the EPR analysis.

Appendix A. Supporting information

Supplementary data associated with this article can be found in the online version at [doi:10.1016/j.apcatb.2023.122791](https://doi.org/10.1016/j.apcatb.2023.122791).

References

- [1] C.S. Deng, Q.Q. Huang, X.Y. Zhu, Q. Hu, W.L. Su, J.N. Qian, L.H. Dong, B. Li, M. G. Fan, C.Y. Liang, The influence of Mn-doped CeO_2 on the activity of CuO/CeO_2 in CO oxidation and NO + CO model reaction, *Appl. Surf. Sci.* 389 (2016) 1033–1049.
- [2] Z.S. Liu, F. Yu, K. Pan, X. Zhou, R.B. Sun, J.Q. Tian, Y.J. Wan, J.M. Dan, B. Dai, Two-dimensional vermiculite carried CuCoCe catalysts for CO-SCR in the presence of O_2 and H_2O : experimental and DFT calculation, *Chem. Eng. J.* 422 (2021), 130099.
- [3] Y.H. Wang, Q.K. Jiang, L.L. Xu, Z.-K. Han, S. Guo, G. Li, A. Baiker, Effect of the configuration of copper oxide–ceria catalysts in NO reduction with CO: Superior performance of copper–ceria solid solution, *ACS Appl. Mater. Interfaces* 13 (2021) 61078–61087.
- [4] C.S. Deng, M. Li, J.N. Qian, Q. Hu, M.N. Huang, Q.J. Lin, Y.S. Ruan, L.H. Dong, B. Li, M.G. Fan, A study of different doped metal cations on the physicochemical properties and catalytic activities of $\text{Ce}_{20}\text{M}_1\text{O}_x$ ($\text{M}=\text{Zr}, \text{Cr}, \text{Mn}, \text{Fe}, \text{Co}, \text{Sn}$) composite oxides for nitric oxide reduction by carbon monoxide, *Chem. -Asian J.* 11 (2016) 2144–2156.
- [5] Z.C. Xu, Y.R. Li, Y.T. Lin, T.Y. Zhu, A review of the catalysts used in the reduction of NO by CO for gas purification, *Environ. Sci. Pollut. Res. Int.* 27 (2020) 6723–6748.
- [6] T. Hirakawa, Y. Shimokawa, W. Tokuzumi, T. Sato, M. Tsushima, H. Yoshida, S. Hinokuma, J. Ohyama, M. Machida, Multicomponent spinel oxide solid solutions: a possible alternative to platinum group metal three-way catalysts, *ACS Catal.* 9 (2019) 11763–11773.
- [7] Y. Zhang, J.C. Lu, L.M. Zhang, T. Fu, J. Zhang, X. Zhu, X.Y. Gao, D.D. He, Y.M. Luo, D.D. Dionysiou, W.J. Zhu, Investigation into the catalytic roles of oxygen vacancies during gaseous styrene degradation process via CeO_2 catalysts with four different morphologies, *Appl. Catal. B: Environ.* 309 (2022), 121249.
- [8] L.J. Yan, Y.Y. Liu, K.W. Zha, H.R. Li, L.Y. Shi, D.S. Zhang, Deep insight into the structure-activity relationship of Nb modified $\text{SnO}_2\text{-CeO}_2$ catalysts for low-temperature selective catalytic reduction of NO by NH_3 , *Catal. Sci. Technol.* 7 (2017) 502–514.
- [9] S.J. Zhan, H.T. Huang, C. He, Y. Xiong, P. Li, S.H. Tian, Controllable synthesis of substitutional and interstitial nitrogen-doped ceria: the effects of doping sites on enhanced catalytic ozonation of organic pollutants, *Appl. Catal. B: Environ.* 321 (2023), 122040.

- [10] J. Yu, Z.C. Si, L. Chen, X.D. Wu, D. Weng, Selective catalytic reduction of NO_x by ammonia over phosphate-containing Ce_{0.75}Zr_{0.25}O₂ solids, *Appl. Catal. B: Environ.* 163 (2015) 223–232.
- [11] L. Zhang, J. Pierce, V.L. Leung, D. Wang, W.S. Epling, Characterization of ceria's interaction with NO_x and NH₃, *J. Phys. Chem. C* 117 (2013) 8282–8289.
- [12] L. Meng, J.-J. Lin, Z.-Y. Pu, L.-F. Luo, A.-P. Jia, W.-X. Huang, M.-F. Luo, J.-Q. Lu, Identification of active sites for CO and CH₄ oxidation over PdO/Ce_{1-x}Pd_xO_{2-δ} catalysts, *Appl. Catal. B: Environ.* 119–120 (2012) 117–122.
- [13] X.B. Huang, K.Y. Zhang, B.X. Peng, G. Wang, M. Muhler, F. Wang, Ceria-based materials for thermocatalytic and photocatalytic organic synthesis, *ACS Catal.* 11 (2021) 9618–9678.
- [14] J.H. M, G.Z. Jin, J.B. Gao, Y.Y. Li, L.H. Dong, M.N. Huang, Q.Q. Huang, B. Li, Catalytic effect of two-phase intergrowth and coexistence CuO–CeO₂, *J. Mater. Chem. A* 3 (2015) 24358–24370.
- [15] Y. Zheng, K.Z. Li, H. Wang, Y.H. Wang, D. Tian, Y.G. Wei, X. Zhu, C.H. Zeng, Y. M. Luo, Structure dependence and reaction mechanism of CO oxidation: a model study on macroporous CeO₂ and CeO₂–ZrO₂ catalysts, *J. Catal.* 344 (2016) 365–377.
- [16] Y. Guan, Y.H. Liu, Q. Lv, B. Wang, Fe decorated CeO₂ microsphere catalyst with surface oxygen defect for NO reduction by CO, *Mol. Catal.* 516 (2021), 111973.
- [17] L. Ilieva, G. Pantaleo, J.W. Sobczak, I. Ivanov, A.M. Venezia, D. Andreeva, NO reduction by CO in the presence of water over gold supported catalysts on CeO₂–Al₂O₃ mixed support, prepared by mechanochemical activation, *Appl. Catal. B: Environ.* 76 (2007) 107–114.
- [18] H. Wang, H.Q. Zhu, Z.F. Qin, G.F. Wang, F.X. Liang, J.G. Wang, Preferential oxidation of CO in H₂ rich stream over Au/CeO₂–Co₃O₄ catalysts, *Catal. Commun.* 9 (2008) 1487–1492.
- [19] C.S. Deng, B. Li, L.H. Dong, F.Y. Zhang, M.G. Fan, G.Z. Jin, J.B. Gao, L.W. Gao, F. Zhang, X.P. Zhou, NO reduction by CO over CuO supported on CeO₂-doped TiO₂: the effect of the amount of a few CeO₂, *Phys. Chem. Chem. Phys.* 17 (2015) 16092–16109.
- [20] C.S. Deng, J.N. Qian, C.X. Yu, Y.N. Yi, P. Zhang, W. Li, L.H. Dong, B. Li, M.G. Fan, Influences of doping and thermal stability on the catalytic performance of CuO/Ce₂₀M₁O_x (M = Zr, Cr, Mn, Fe, Co, Sn) catalysts for NO reduction by CO, *RSC Adv.* 6 (2016) 113630–113647.
- [21] Y.L. Wang, X.C. Jiang, Y.N. Xia, A solution-phase, precursor route to polycrystalline SnO₂ nanowires that can be used for gas sensing under ambient conditions, *J. Am. Chem. Soc.* 125 (2003) 16176–16177.
- [22] W.X. Zhao, J. Rong, W. Luo, L.L. Long, X.J. Yao, Enhancing the K-poisoning resistance of CeO₂–SnO₂ catalyst by hydrothermal method for NH₃–SCR reaction, *Appl. Surf. Sci.* 579 (2022), 152176.
- [23] X.J. Yao, Y. Xiong, W.X. Zou, L. Zhang, S.G. Wu, X. Dong, F. Gao, Y. Deng, C. J. Tang, Z. Chen, L. Dong, Y. Chen, Correlation between the physicochemical properties and catalytic performances of Ce_xSn_{1-x}O₂ mixed oxides for NO reduction by CO, *Appl. Catal. B: Environ.* 144 (2014) 152–165.
- [24] M.E. Yu, C.T. Li, G.M. Zeng, Y. Zhou, X.N. Zhang, Y.E. Xie, The selective catalytic reduction of NO with NH₃ over a novel Ce–Sn–Ti mixed oxides catalyst: Promotional effect of SnO₂, *Appl. Surf. Sci.* 342 (2015) 174–182.
- [25] W. Tan, S.H. Xie, X. Wang, J.T. Xu, Y. Yan, K.L. Ma, Y.D. Cai, K.L. Ye, F. Gao, L. Dong, F.D. Liu, Determination of intrinsic active sites on CuO–CeO₂–Al₂O₃ catalysts for CO oxidation and NO reduction by CO: Differences and connections, *ACS Catal.* 12 (2022) 12643–12657.
- [26] R.H. Gao, D.S. Zhang, P. Maitrad, L.Y. Shi, T. Rungratmongkol, H.R. Li, J. P. Zhang, W.G. Cao, Morphology-dependent properties of Mn₂O₃/ZrO₂–CeO₂ nanostructures for the selective catalytic reduction of NO with NH₃, *J. Phys. Chem. C* 117 (2013) 10502–10511.
- [27] S.J. Clark, M.D. Segall, C.J. Pickard, P.J. Hasnip, M.I.J. Probert, K. Refson, M. C. Payne, First principles methods using CASTEP, *Z. Krist.* 220 (2005) 567–570.
- [28] T.H. Fischer, J. Almlöf, General methods for geometry and wave function optimization, *J. Phys. Chem.* 96 (1992) 9768–9774.
- [29] Z.L. Wu, M.J. Li, S.H. Overbury, On the structure dependence of CO oxidation over CeO₂ nanocrystals with well-defined surface planes, *J. Catal.* 285 (2012) 61–73.
- [30] Y. Wang, A.M. Zhu, Y.Z. Zhang, C.T. Au, X.F. Yang, C. Shi, Catalytic reduction of NO by CO over NiO/CeO₂ catalyst in stoichiometric NO/CO and NO/CO/O₂ reaction, *Appl. Catal. B: Environ.* 81 (2008) 141–149.
- [31] X.J. Yao, Q. Yu, Z.Y. Ji, Y.Y. Lv, Y. Cao, C.J. Tang, F. Gao, L. Dong, Y. Chen, A comparative study of different doped metal cations on the reduction, adsorption and activity of CuO/Ce_{0.67}M_{0.33}O₂ (M = Zr⁴⁺, Sn⁴⁺, Ti⁴⁺) catalysts for NO + CO reaction, *Appl. Catal. B: Environ.* 130–131 (2013) 293–304.
- [32] C.S. Deng, Y. Cui, J.C. Chen, T. Chen, X.F. Guo, W.J. Ji, L.M. Peng, W.P. Ding, Enzyme-like mechanism of selective toluene oxidation to benzaldehyde over organophosphoric acid-bonded nano-oxides, *Chin. J. Catal.* 42 (2021) 1509–1518.
- [33] C.S. Deng, M.X. Xu, Z. Dong, L. Li, J.Y. Yang, X.F. Guo, L.M. Peng, N.H. Xue, Y. Zhu, W.P. Ding, Exclusively catalytic oxidation of toluene to benzaldehyde in an O/W emulsion stabilized by hexadecylphosphate acid terminated mixed-oxide nanoparticles, *Chin. J. Catal.* 41 (2020) 341–349.
- [34] C.S. Deng, K. Wang, X.F. Qian, J. Yao, N.H. Xue, L.M. Peng, X.F. Guo, Y. Zhu, W. P. Ding, Mild oxidation of toluene to benzaldehyde by air, *Ind. Eng. Chem. Res* 62 (2023) 1688–1694.
- [35] C.J. Tang, J.C. Li, X.J. Yao, J.F. Sun, Y. Cao, L. Zhang, F. Gao, Y. Deng, L. Dong, Mesoporous NiO–CeO₂ catalysts for CO oxidation: Nickel content effect and mechanism aspect, *Appl. Catal. A: Gen.* 494 (2015) 77–86.
- [36] Y. She, Q. Zheng, L. Li, Y. Zhan, C. Chen, Y. Zheng, X. Lin, Rare earth oxide modified CuO/CeO₂ catalysts for the water–gas shift reaction, *Int. J. Hydrog. Energy* 34 (2009) 8929–8936.
- [37] H. Vidal, J. Kašpar, M. Pijolat, G. Colon, S. Bernal, A. Cordón, V. Perrichon, F. Fally, Redox behavior of CeO₂–ZrO₂ mixed oxides I. Influence of redox treatments on high surface area catalysts, *Appl. Catal. B: Environ.* 27 (2000) 49–63.
- [38] L. Ilieva, G. Pantaleo, I. Ivanov, A.M. Venezia, D. Andreeva, Gold catalysts supported on CeO₂ and CeO₂–Al₂O₃ for NO_x reduction by CO, *Appl. Catal. B: Environ.* 65 (2006) 101–109.
- [39] X.J. Yao, C.J. Tang, Z.Y. Ji, Y. Dai, Y. Cao, F. Gao, L. Dong, Y. Chen, Investigation of the physicochemical properties and catalytic activities of Ce_{0.67}M_{0.33}O₂ (M = Zr⁴⁺, Ti⁴⁺, Sn⁴⁺) solid solutions for NO removal by CO, *Catal. Sci. Technol.* 3 (2013) 688–698.
- [40] B.M. Reddy, P. Bharali, P. Saikia, S.E. Park, M.W.E. Van den Berg, M. Muhler, W. Grinert, Structural characterization and catalytic activity of nanosized Ce_xM_{1-x}O₂ (M = Zr and Hf) mixed oxides, *J. Phys. Chem. C* 112 (2008) 11729–11737.
- [41] J.C. Chen, M.A. Hope, Z.Y. Lin, M. Wang, T. Liu, D.M. Halat, Y.J. Wen, T. Chen, X. K. Ke, P.C.M.M. Magusin, W.P. Ding, X.F. Xia, X.-P. Wu, X.-Q. Gong, C.P. Grey, L. M. Peng, Interactions of oxide surfaces with water revealed with solid-state NMR spectroscopy, *J. Am. Chem. Soc.* 142 (2020) 11173–11182.
- [42] Y.Y. Cui, W.-L. Dai, Support morphology and crystal plane effect of Cu/CeO₂ nanomaterial on the physicochemical and catalytic properties for carbonate hydrogenation, *Catal. Sci. Technol.* 6 (2016) 7752–7762.
- [43] Y. Pua, Y.D. Luo, X.Q. Wei, J.F. Sun, L.L. Li, W.X. Zou, L. Dong, Synergistic effects of Cu₂O-decorated CeO₂ on photocatalytic CO₂ reduction: surface Lewis acid/base and oxygen defect, *Appl. Catal. B: Environ.* 254 (2019) 580–586.
- [44] N.X. Li, X.Y. Zou, M. Liu, L.F. Wei, Q.H. Shen, R. Bibi, C.J. Xu, Q.H. Ma, J.C. Zhou, Enhanced visible light photocatalytic hydrogenation of CO₂ into methane over a Pd/Ce-TiO₂ nanocomposition, *J. Phys. Chem. C* 121 (2017) 25795–25804.
- [45] X.-Y. Yang, Y.-T. Shi, F.-L. Gong, J.-L. Chen, G.-X. Jin, Q. Guo, H.-L. Zhang, Y.-H. Zhang, Asymmetric interfacial oxygen sites of porous CeO₂–SnO₂ nanosheets enabling highly sensitive and selective detection of 3-hydroxy-2-butaneone biomarkers, *Sens. Actuat.: B. Chem.* 371 (2022), 132500.
- [46] K. Shimizu, H. Kawachi, S. Komai, K. Yoshida, Y. Sasaki, A. Satsuma, Carbon oxidation with Ag/ceria prepared by self-dispersion of Ag powder into nanoparticles, *Catal. Today* 175 (2011) 93–99.
- [47] X.X. Wang, B.B. Chen, G.Z. Chen, X. Sun, Oxygen vacancies dependent Au nanoparticle deposition and CO oxidation, *RSC Adv.* 6 (2016) 87978–87987.
- [48] Y.G. Wang, F. Wang, Y.T. Chen, D.F. Zhang, B. Li, S.F. Kang, X. Li, L.F. Cui, Enhanced photocatalytic performance of ordered mesoporous Fe-doped CeO₂ catalysts for the reduction of CO₂ with H₂O under simulated solar irradiation, *Appl. Catal. B: Environ.* 147 (2014) 602–609.
- [49] G. Avgouropoulos, T. Ioannides, Effect of synthesis parameters on catalytic properties of CuO–CeO₂, *Appl. Catal. B: Environ.* 67 (2006) 1–11.
- [50] M. Boaro, F. Giordano, S. Recchia, V. Dal Santo, M. Giona, A. Trovarelli, On the mechanism of fast oxygen storage and release in ceria-zirconia model catalysts, *Appl. Catal. B: Environ.* 52 (2004) 225–237.
- [51] N. Murata, T. Suzuki, Y. Lin, H. Nitani, Y. Niwa, T. Wada, M. Uo, K. Asakura, Structure of atomically dispersed Pt in a SnO₂ thin film under reaction conditions: Origin of its high performance in micro electromechanical system gas sensor catalysis, *ACS Appl. Mater. Interfaces* 14 (2022) 39507–39514.
- [52] S.H. Xie, W. Tan, Y.J. Li, L. Ma, S.N. Ehrlich, J.G. Deng, P. Xu, F. Gao, L. Dong, F. D. Liu, Copper single atom-triggered niobia–ceria catalyst for efficient low-temperature reduction of nitrogen oxides, *ACS Catal.* 12 (2022) 2441–2453.
- [53] L.J. Liu, J.G. Cai, L. Qi, Q. Yu, K.Q. Sun, B. Liu, F. Gao, L. Dong, Y. Chen, Influence of supports structure on the activity and adsorption behavior of copper-based catalysts for NO reduction, *J. Mol. Catal. A: Chem.* 327 (2010) 1–11.
- [54] C.Z. Sun, J. Zhu, Y.Y. Lv, L. Qi, B. Liu, F. Gao, K.Q. Sun, L. Dong, Y. Chen, Dispersion, reduction and catalytic performance of CuO supported on ZrO₂-doped TiO₂ for NO removal by CO, *Appl. Catal. B: Environ.* 103 (2011) 206–220.
- [55] L.J. Liu, B. Liu, L.H. Dong, J. Zhu, H.Q. Wan, K.Q. Sun, B. Zhao, H.Y. Zhu, L. Dong, Y. Chen, In situ FT-infrared investigation of CO or/and NO interaction with CuO/Ce_{0.67}Zr_{0.33}O₂ catalysts, *Appl. Catal. B: Environ.* 90 (2009) 578–586.
- [56] D. Li, Q. Yu, S.S. Li, H.Q. Wan, L.J. Liu, L. Qi, B. Liu, F. Gao, L. Dong, Y. Chen, The remarkable enhancement of CO-pre-treated CuO–Mn₂O₃/γ-Al₂O₃ supported catalyst for the reduction of NO with CO: the formation of surface synergistic oxygen vacancy, *Chem. Eur. J.* 17 (2011) 5668–5679.
- [57] H. Liu, L.H. Liu, L.Q. Wei, B.X. Chu, Z.Z. Qin, G.Z. Jin, Z.F. Tong, L.H. Dong, B. Li, Preparation of three-dimensionally ordered macroporous MFe₂O₄ (M = Co, Ni, Cu) spinel catalyst and its simultaneous catalytic application in CO oxidation and NO + CO reaction, *Fuel* 272 (2020), 117738.
- [58] T.K. Liu, Y.Y. Yao, L.Q. Wei, Z.F. Shi, L.Y. Han, H.X. Yuan, B. Li, L.H. Dong, F. Wang, C.Z. Sun, Preparation and evaluation of copper–manganese oxide as a high-efficiency catalyst for CO oxidation and NO reduction by CO, *J. Phys. Chem. C* 121 (2017) 12757–12770.